REVIEW

Recent progress in two-dimensional Bi_2O_2Se and its heterostructures

Xiaoyu Hu, [ID] [a] Wen He, [ID] *[a] Dongbo Wang, [ID] *[a] Lei Chen,[a] Xiangqian Fan,[a] Duoduo Ling,[a] Yanghao Bi,[a] Wei Wu,[a] Shuai Ren,[a] Ping Rong,[a] Yinze Zhang,[a] Yajie Han[a] and Jinzhong Wang*[a,b,c]

Ever since the identification of graphene, research on two-dimensional (2D) materials has garnered significant attention. As a typical layered bismuth oxyselenide, Bi_2O_2Se has attracted growing interest not only due to its conventional thermoelectricity but also because of the excellent optoelectronic properties found in the 2D limit. Moreover, 2D Bi_2O_2Se exhibits remarkable properties, including high carrier mobility, air stability, tunable band gap, unique defect characteristics, and favorable mechanical properties. These properties make it a promising candidate for next-generation electronic and optoelectronic devices, such as logic devices, photodetectors, sensors, energy technologies, and memory devices. However, despite significant progress, there are still challenges that must be addressed for widespread commercial use. This review provides an overview of progress in Bi_2O_2Se research. We start by introducing the crystal structure and physical properties of Bi_2O_2Se and a compilation of methods for modulating its physical properties is further outlined. Then, a series of methods for synthesizing high-quality 2D Bi_2O_2Se are summarized and compared. We next focus on the advancements made in the practical applications of Bi_2O_2Se in the fields of field-effect transistors (FETs), photodetectors, neuromorphic computing and optoelectronic synapses. As heterostructures induce a new degree of freedom to modulate the properties and broaden applications, we especially discuss the heterostructures and corresponding applications of Bi_2O_2Se integrated with 0D, 1D and 2D materials, providing insights into constructing heterojunctions and enhancing device performance. Finally, the development prospects for Bi_2O_2Se and future challenges are discussed.

1. Introduction

As the size of silicon transistors approaches its physical limit, Moore's law is gradually becoming invalid. Currently, scaling is becoming increasingly challenging due to the significant increase in chip power density and the severe degradation of gate electrostatics. To address this issue, a significant reduction in channel thickness is required. On the other hand, with the advancement of the intelligent era, the demand for multifunctional sensors, photodetectors, and wearable devices is growing. For example, there are photodetectors for detecting infrared and visible light,[1,2] gas sensors for monitoring the environment,[3–5] and bio-sensors for monitoring various health

indicators of the body.[6] 2D materials have shown promising potential applications in these areas. A 2D material is a material in which the bonding strength is similar along two directions and far greater than that in the third dimension.[7] The unique crystalline structure of 2D materials enables the manipulation of their properties through a variety of methods. These methods include defect engineering, applying external pressure/stress/magnetic fields, and constructing heterojunctions.[8–10] In addition to graphene, there are a variety of 2D materials, covering almost all kinds of electronic structures, such as transition metal dichalcogenides (TMDs), black phosphorus (BP), boron nitride (BN), graphitic carbon nitride, MXenes, monolayer elements, metal phosphorus trichalcogenides, layered double hydroxides and their heterostructures, which have been a hot topic in recent years.[11]

Despite many studies that have demonstrated the unique properties of 2D materials, several inherent limitations still impede their further development. For instance, at room temperature, graphene exhibits ultrahigh carrier mobility exceeding $10\,000\ \mathrm{cm^2\ V^{-1}\ s^{-1}}$. Nevertheless, the lack of a band gap results in a limited on/off current ratio for FETs and low light

[a]*School of Materials Science and Engineering, Harbin Institute of Technology, Harbin, China. E-mail: hewenmse@hit.edu.cn, wangdongbo@hit.edu.cn, jinzhong_wang@hit.edu.cn*
[b]*State Key Laboratory of Precision Welding and Joining of Materials and Structures, Harbin, 150001, China*
[c]*Heilongjiang Provincial Key Laboratory of Advanced Quantum Functional Materials and Sensor Devices, Harbin 150001, China*

absorption in the visible spectrum.[12] BP has a tunable band gap and promising carrier mobility,[13] but its poor air stability seriously hinders its practical applications.[14] For TMDs, their relatively slow carrier mobility (approximately 200 cm^2 V^{-1} s^{-1}) and wide band gaps make them unsuitable as high-speed photodetectors.[15]

Thus, researchers are eager to explore new materials with high carrier mobility, excellent air stability, and tunable band gaps. Air-stable bismuth oxychalcogenides (Bi$_2$O$_2$X, X = S, Se, Te) have shown exceptional electrical and optoelectronic properties, making them promising candidates for high-performance devices. Among them, Bi$_2$O$_2$S, with its orthorhombic crystal structure (space group *Pnnm*), offers distinct advantages, including efficient charge separation, high charge carrier transport, and long carrier lifetimes. Additionally, its elements are abundant in nature and environment-friendly, making it a promising material for sustainable technologies. Numerous studies have demonstrated the excellent performance of Bi$_2$O$_2$S in advanced optoelectronic devices.[16–18] Bi$_2$O$_2$Te is predicted to have the smallest effective mass within the Bi$_2$O$_2$X family, along with enhanced spin–orbit coupling and the potential for ferroelectricity under in-plane stress. These properties suggest the potential for rich physical phenomena and superior electrical performance. Although the narrow chemical potential window of Bi$_2$O$_2$Te and the relatively inert chemical reactivity of Te present significant challenges for its synthesis,[19] several epitaxial methods have been proposed to synthesize high-mobility Bi$_2$O$_2$Te nanosheets.[20,21] Moreover, the native thermal oxidation behaviour of Bi$_2$O$_2$Te to Bi$_2$O$_6$Te has also been reported.[22] Bi$_2$O$_2$Se is the first member of the Bi$_2$O$_2$X family to be discovered, and due to its easier synthesis compared to other members, it has become the most extensively studied material in this group. It demonstrates promising carrier mobility, a tunable band gap, superior air stability, and numerous modulation methods, making it a strong contender for next-generation devices. Additionally, Bi$_2$O$_2$Se exhibits distinctive silicon-like properties, allowing it to self-oxidize into a dense, conformal, high-k native oxide known as Bi$_2$SeO$_5$,[23] which can be directly used as a gate insulator.

Previous studies predominantly focused on the applications of bulk Bi$_2$O$_2$Se in the thermoelectric field, while the exceptional electronic properties of its ultrathin structure were overlooked. It was only recently that the synthesis and in-depth investigation of its ultrathin structure commenced. A wide range of methods can be used to prepare 2D Bi$_2$O$_2$Se, including chemical vapor deposition (CVD),[24–28] molecular beam epitaxy (MBE)[29] and so on. The synthesis of Bi$_2$O$_2$Se with different morphologies provides researchers with a wide range of opportunities to explore its potential applications. Bi$_2$O$_2$Se nanoplates are highly stable in air and have an exceptionally high Hall mobility of 28 900 cm^2 V^{-1} s^{-1} at 1.9 K. FETs made from Bi$_2$O$_2$Se exhibit a remarkable performance, with a large on/off current ratio (>10^6) and a nearly ideal subthreshold swing of ≈65 mV dec^{-1}.[30] The band gap of 2D Bi$_2$O$_2$Se is 0.8 eV, which makes it a promising material for infrared (IR) photodetection. The IR photodetector based on Bi$_2$O$_2$Se shows a response time of 2.8 ms, a responsivity of 6.5 A W^{-1}, and a detectivity of 8.3 × 10^{11} Jones.[31] Furthermore, strong Shubnikovde Haas (SdH) quantum oscillation[24] and strong spin–orbital interactions[32] are observed in Bi$_2$O$_2$Se nanolayers, which indicate potential applications in topological quantum devices and spintronics. The atomic-level thickness of Bi$_2$O$_2$Se nanosheets facilitates the construction of heterojunctions, allowing for precise modulation of device performance.[33] Additionally, the interlayer electrostatic interactions within Bi$_2$O$_2$Se nanosheets significantly enhance the interaction between different layers, stabilizing the heterojunction structure and improving both electronic and optical properties.[34,35] These superior characteristics make Bi$_2$O$_2$Se a compelling candidate for designing low-cost, high-performance devices.

Aiming to reveal the wonders of Bi$_2$O$_2$Se, we first introduce its crystal structure and fundamental properties, followed by summarizing a series of methods for tuning its physical

Xiaoyu Hu is a fourth-year undergraduate student at the School of Materials Science and Engineering, Harbin Institute of Technology, majoring in optoelectronic information materials and devices. His research focuses on the epitaxial growth of 2D materials and their applications in photodetectors.

Xiaoyu Hu

He Wen is an assistant professor at the School of Materials Science and Engineering, Harbin Institute of Technology. She received her Ph.D. degree in materials science and engineering from the National University of Singapore in 2021. Then she worked at the National University of Singapore as a postdoc until 2023 before joining the Harbin Institute of Technology. Her current research interests are first-principles calculations of the optical properties of two-dimensional materials and their optoelectronics.

Wen He

characteristics. Subsequently, we elaborate on various synthesis methods of Bi_2O_2Se, including approaches for their improvement. Finally, we discuss the applications of Bi_2O_2Se in FETs, photodetectors, lasers, and neuromorphic computing. Additionally, we observe a lack of comprehensive reviews on the construction of heterostructures involving Bi_2O_2Se in the literature. However, the simplicity of constructing heterostructures is precisely one of the major advantages of 2D materials over others. Therefore, the final section emphasizes research on the construction of heterostructures involving 2D Bi_2O_2Se and their corresponding applications. By examining these aspects, we aim to highlight the significance of Bi_2O_2Se and its role in advancing various technological fields.

2. Structures

2.1. Crystal structures

Layered Bi_2O_2Se features a tetragonal crystal structure with the $I4/mmm$ space group, as shown in Fig. 1a.[25] This structure is considered quasi-2D. The lattice parameters are $a = b = 3.887$ Å and $c = 12.164$ Å. The tetragonal lattice is formed by the arrangement of O atoms, with Bi atoms occupying the tetragonal interstitial sites above and below these O atoms, forming $[Bi_2O_2]^{2+}$ layers. Se atoms are located in interstitial sites, with weak electrostatic interactions binding the $[Bi_2O_2]^{2+}$ layers together. The lattice structure of Bi_2O_2Se has been revealed by high-angle annular dark-field scanning transmission electron microscopy (HAADF-STEM), as shown in Fig. 1b.[36] The layer thickness of Bi_2O_2Se is exactly half of the c parameter (6.1 Å), which is clear evidence that Bi_2O_2Se grows in layers.[30] The layered structure of Bi_2O_2Se induces anisotropic optical, mechanical, and electronic properties in in-plane and out-of-plane directions.[37] Wei *et al.*[38] proposed that Bi_2O_2Se could be classified as a "zipper 2D" material (Fig. 1c) based on theoretical and experimental studies. This model is similar to zippers, demonstrating that the upper and lower surfaces of layered Bi_2O_2Se have 50% Se coverage (Fig. 1d). Furthermore, it proves that the interactions between $[Bi_2O_2]_n^{2n+}-[Se]_n^{2n-}$ layers involve electrostatic forces instead of vdW forces[24,38] so chemical bonds near the surface in single-layer Bi_2O_2Se are stronger than those of conventional 2D materials such as graphene[12] and $MoSe_2$.[11] Its high interlayer binding energy makes Bi_2O_2Se more difficult to mechanically exfoliate than other 2D materials.

2.2. Electronic structures

With the development of Bi_2O_2Se preparation technology, ultrathin 2D materials have been obtained, and thus many of its physical properties have been revealed. The band structure and density of states in bulk Bi_2O_2Se crystals were investigated using both first-principles calculations and angle-resolved photoemission spectroscopy (ARPES) measurements (Fig. 1e and f). It was found that the electronic states near the conduction band minimum at the Γ point originated from the Bi p-orbital bands and exhibited a strong dispersion along the Γ–X and Γ–M directions. This dispersion causes Bi_2O_2Se to exhibit properties that are sensitive to thickness, leading to a size-tunable band gap as the material is thinned toward the monolayer limit due to quantum confinement effects.[24] Notably, the band gap of Bi_2O_2Se decreases as the thickness increases. However, the band gap decrease from monolayer to bilayer Bi_2O_2Se is significantly larger than that from the bilayer to more layers (Fig. 1g).[38] Furthermore, ARPES distinctly unveiled an indirect band gap of approximately 0.8 eV, matching well with the computed value of around 0.85 eV.[24] Moreover, a remarkably low in-plane electron effective mass of $m^* = 0.14 \pm 0.02m_0$ (m_0 is the free-electron mass) was determined by fitting the conduction band, as revealed by ARPES (Fig. 1f). Notably, this m^* value is lower than those observed in silicon ($0.26m_0$),[39] MoS_2 ($0.4–0.6m_0$),[40,41] and BP ($0.15m_0$ for

Dongbo Wang

Dongbo Wang is a professor at the School of Materials Science and Engineering, Harbin Institute of Technology. He obtained his bachelor's degree from the Changchun University of Science and Technology in 2006, majoring in optoelectronic information science and engineering. He obtained his master's degree, majoring in materials physics and chemistry, from the Harbin Institute of Technology in 2009, and his PhD degree in optoelectronic information science and engineering from the Harbin Institute of Technology in 2013. His research interests focus on the study of UV and IR detection materials and hydrogen production from the solar photolysis of water.

Jinzhong Wang

Jinzhong Wang is a professor at the School of Materials Science and Engineering, Harbin Institute of Technology. He obtained his Ph.D. from the School of Electronic Engineering at Jilin University in 2002. He worked as a researcher in France at the Bellevue Laboratory in 2003, and from 2004 to 2009, he was a postdoctoral researcher in Portugal, first at the University of Aveiro and then at the New University of Lisbon. He joined the Harbin Institute of Technology in 2009 specializing in the development and fabrication of novel luminescent thin-film materials.
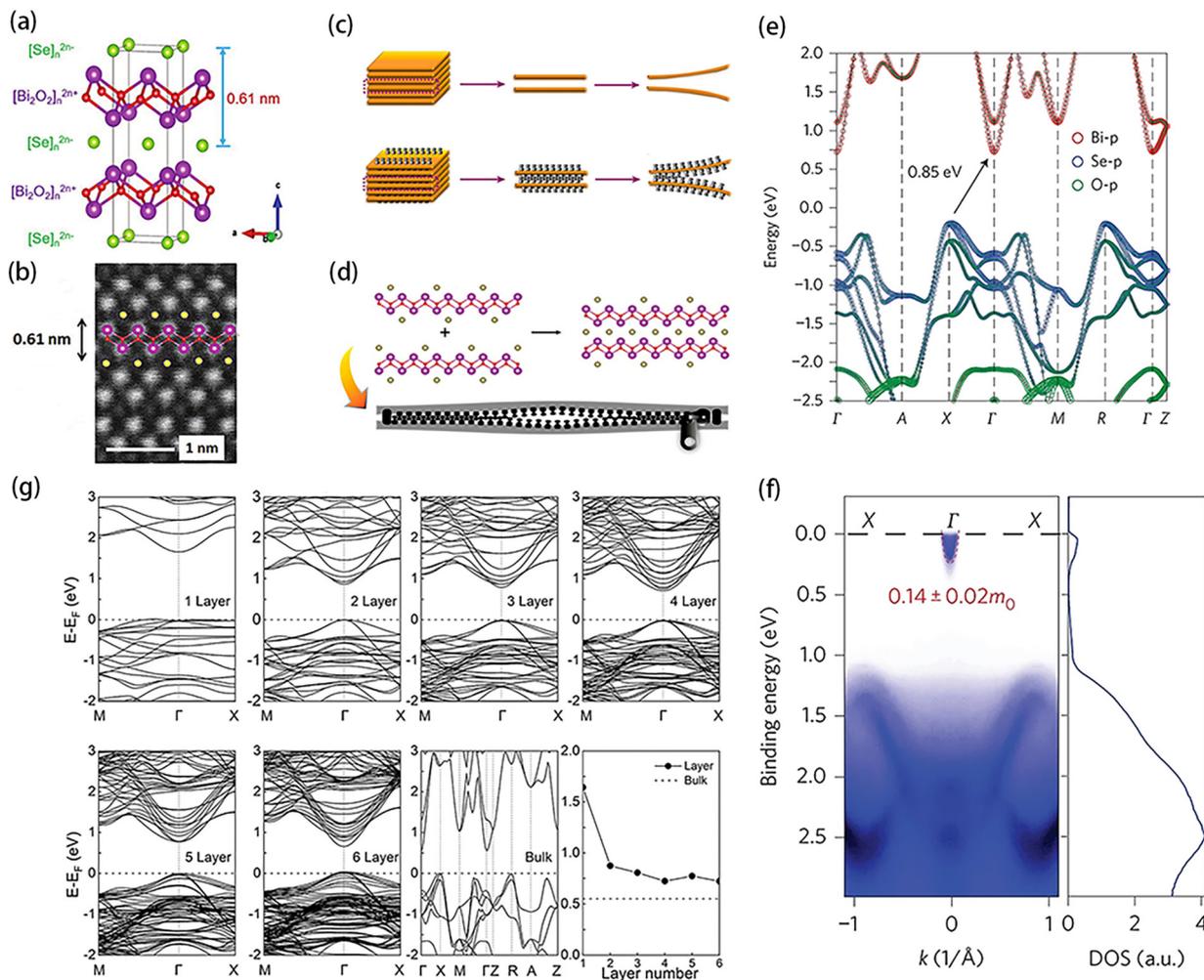
Review

Nanoscale

Fig. 1 Crystal and electronic structures of Bi_2O_2Se. (a) Schematic of the crystal structure of layered Bi_2O_2Se. Reproduced with permission.[25] Copyright 2018, Wiley. (b) Cross-sectional HAADF-STEM image of a Bi_2O_2Se film, showing a layer thickness of 0.61 nm. Reproduced with permission.[36] Copyright 2020, Wiley. (c) Illustrations depicting vdW and zipper 2D materials. (a and b) Representations of bulk and bilayer configurations for vdW 2D materials; (d and e) bulk and bilayer arrangements for zipper 2D materials. (d) Schematic of a zipper 2D model of Bi_2O_2Se. (e) Theoretical band structure of Bi_2O_2Se, with a band gap of 0.85 eV. (f) Measurements of band dispersion and density of states (DOS). (e and f) Reproduced with permission.[24] Copyright 2017, Springer Nature. (g) Calculated band structures of Bi_2O_2Se with 1–6 layers. (c, d and g) Reproduced with permission.[38] Copyright 2019, American Chemical Society.

m_x^*, $1.18m_0$ for m_y^*, where m_x and m_y represent the effective mass of charge carriers along the armchair direction and zigzag direction of BP, respectively).[42] This suggests the potential for achieving ultrahigh electron mobility.

2.3. Physical properties

Due to its special structure, Bi_2O_2Se has many intriguing physical properties. Extensive theoretical and experimental investigations have been conducted to reveal these characteristics, which include ultrahigh Hall mobility,[24] thickness-dependent mobility,[24] strong spin–orbit interactions,[32,43] and outstanding optical properties.[44]

A Hall-bar device was directly fabricated using CVD-grown 2D Bi_2O_2Se, as reported by Wu et al.[24] The electron Hall mobility of non-encapsulated Bi_2O_2Se flakes reached values of

18 500–28 900 cm² V⁻¹ s⁻¹ at 1.9 K (Fig. 2a). As shown in Fig. 2b, the mobility is relatively stable when the thickness is beyond 6 nm, while it decreases significantly with decreasing thickness when the thickness is less than 6 nm. From this study, it is evident that the electron mobility of Bi_2O_2Se is significantly influenced by its thickness. Enhanced device performance can be achieved through precise thickness control and suppression of electron scattering at the surface/interface. The Rashba splitting effect has also been revealed in Bi_2O_2Se thin films under strong magnetic fields.[45] When Bi_2O_2Se is grown on $SrTiO_3$ with a thickness of 6 unit cells (uc, 1 uc of Bi_2O_2Se consists of two layers), only even-integer quantum Hall states are observed in magnetic fields up to 50 T, with no indication of odd-integer states. This can be attributed to a hidden Rashba effect, where local inversion symmetry break-
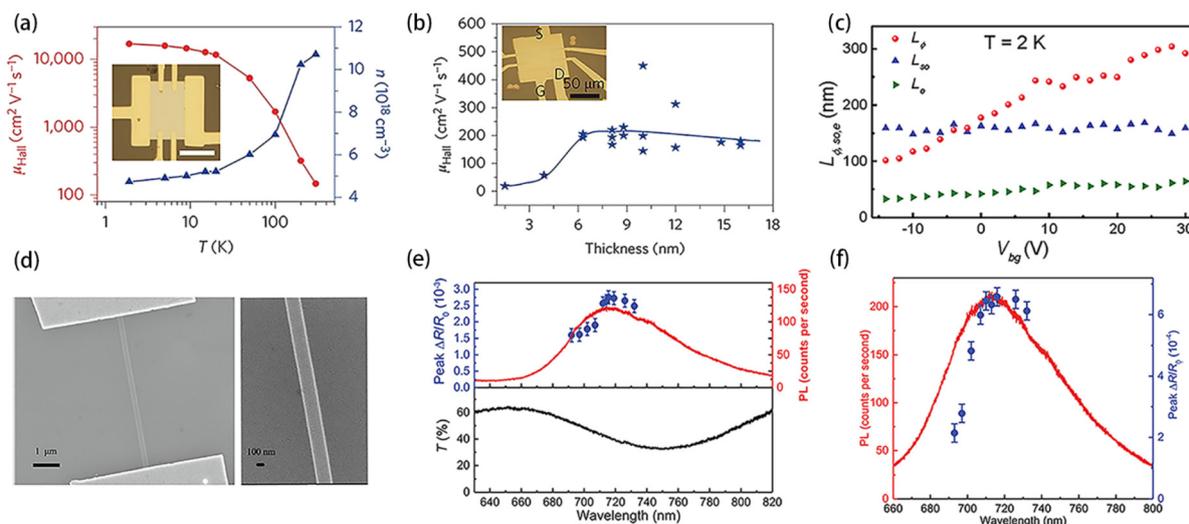
Fig. 2 Physical and optical properties of Bi_2O_2Se. (a) The relationship between Hall mobility and carrier concentration in Bi_2O_2Se nanosheets revealed by Hall effect measurements. The inset shows a schematic of the Hall bar device used in the measurements, which is based on a Bi_2O_2Se nanosheet with a thickness of ≈ 20 nm. (b) Experimentally determined Hall mobility of CVD-grown Bi_2O_2Se at room temperature across flake thicknesses from 1.5 to 16 nm. (a and b) Reproduced with permission.[24] Copyright 2017, Springer Nature. (c) L_ϕ, L_{so}, and L_e of the device as a function of back gate voltage (V_{bg}). Reproduced with permission.[32] Copyright 2018, Royal Society of Chemistry. (d) Scanning electron microscope (SEM) image of the measured device (left panel): a Bi_2O_2Se nanowire in contact with two Ti/Au electrodes. Magnified image of the nanowire (right panel). Reproduced with permission.[43] Copyright 2022, AIP Publishing. (e) Peak differential reflection of 13 nm thick Bi_2O_2Se nanosheets (blue dots), photoluminescence spectrum (red curve) excited by a 532 nm laser, and transmission spectrum of the nanosheets (black curve). (f) Peak differential reflection (blue dots) and transmission spectra (red curve) of monolayer Bi_2O_2Se. (e and f) Reproduced with permission.[44] Copyright 2020, Wiley.

ing in the two sectors of the $[Bi_2O_2]^{2+}$ layers generates opposite Rashba spin polarizations, which cancel each other out. However, when the thickness is reduced to 1 uc, a significant global Rashba splitting emerges due to inversion symmetry breaking in the Janus Bi_2O_2Se film, with a value of 440 meV, one of the largest values reported for 2D semiconductor Rashba systems.[46–48] This strong Rashba effect lifts the electronic degeneracy, resulting in the coexistence of both odd and even quantum Hall states. These characteristics position 2D Bi_2O_2Se as a promising platform for exploring Rashba-related physics and designing novel spintronic devices at the atomic scale.

Strong spin–orbit interactions are also found in both Bi_2O_2Se nanoplates and nanowires.[32,43] Meng *et al.*[32] measured the low-field magnetoconductivity of nanosheets at different carrier densities. Their study indicated a carrier mean-free path, denoted as L_e, of approximately 35 nm at 2 K. Additionally, systematic explorations were conducted to measure the dephasing length (L_ϕ), spin relaxation length (L_{so}), and L_e in relation to the back gate voltage. Their results (Fig. 2c) showed that L_{so} obtained in the nanosheets was 150 nm, which was shorter than that in $Al_xGa_{1-x}N$/GaN 2DEG (~290 nm)[49] and InSb nanowires (~250 nm).[50] Zhao *et al.*[43] conducted systematic studies on the electrical transport properties of CVD-grown Bi_2O_2Se nanowires (Fig. 2d). The nanowires showed a high mobility of up to 1.34×10^4 cm^2 V^{-1} s^{-1}, which was larger than that of 2D flakes and a gate-tunable spin–orbit coupling (SOC). They identified two types of carrier in their Bi_2O_2Se nanowires: surface accumu-

lation carriers and internal stacking layer carriers. The surface accumulation carriers exhibited strong inversion asymmetry, which led to strong SOC in the nanowires. Nanowires exhibit ballistic transport at low back gate voltages, while it translates into phase-coherent transport at higher back gate voltages, where weak antilocalization (WAL)[51] is observed.

Bi_2O_2Se also exhibits excellent optoelectronic properties, laying the foundation for its applications in advanced optoelectronic devices. The photoluminescence (PL) spectra excited by a 532 nm laser and the peak differential reflectance and transmission spectra of 13 nm thick and monolayer Bi_2O_2Se nanosheets were analyzed,[44] as depicted in Fig. 2e and f. According to first-principles calculations of monolayer Bi_2O_2Se, the peak of the PL spectrum, approximately at 720 nm (1.72 eV), was attributed to transitions between conduction and valence band states at the Γ point.[52] Time-resolved differential reflectance measurements revealed a carrier recombination lifetime of approximately 200 ps in the nanosheets, accompanied by a carrier diffusion coefficient of 4.8 cm^2 s^{-1}, corresponding to a mobility of approximately 180 cm^2 V^{-1} s^{-1}. In contrast, the diffusion coefficient of excitons in monolayer Bi_2O_2Se films was around 20 cm^2 s^{-1}, several times higher than that in Bi_2O_2Se nanosheets, indicating the significant influence of thickness on the physical properties of 2D Bi_2O_2Se.

The observed characteristics, including tunable band gap, high electron mobility, and excellent optoelectronic properties, make Bi_2O_2Se a promising candidate for a wide range of

advanced technologies, from high-performance transistors to novel quantum devices.[49,53]

3. Physical property modulation

Bi$_2$O$_2$Se, as a distinctive semiconductor material, exhibits variations in its properties under different thicknesses.[24,38] Furthermore, the density of defects, along with external stress and pressure, can also significantly influence its electrical characteristics.[24,54,55] Herein, we present a comprehensive analysis of how thickness, pressure, defects, and stress affect the physical properties of Bi$_2$O$_2$Se and introduce studies on various modulation techniques.

3.1. Thickness control

As mentioned above, the electrical and optoelectronic properties of Bi$_2$O$_2$Se are significantly dependent on the thickness. Variations in thickness result in notable changes to the electron mobility, band gap, optical absorption, and mechanical properties, underscoring the crucial role of thickness in modulating the properties of 2D Bi$_2$O$_2$Se.[38,44,56] Therefore,

precise control over thickness would greatly expand the potential applications of Bi$_2$O$_2$Se. Due to its stronger interlayer binding energy compared to van der Waals materials, the mechanical exfoliation of Bi$_2$O$_2$Se for thickness control is challenging. Therefore, alternative methodologies are imperative for achieving precise thickness modulation. The most common and widely employed approach is controlling the growth conditions.

The thickness of Bi$_2$O$_2$Se nanosheets exhibits a pronounced dependence on growth temperature and pressure. Fan *et al.*[53] prepared Bi$_2$O$_2$Se nanosheets with thicknesses of 8 nm and over 40 nm by controlling the conditions of CVD growth. At 560 °C, under a pressure of 700 Pa, visibly darker and larger thick nanosheets were observed, as depicted in Fig. 3a (left panel). Conversely, by reducing the pressure to 600 Pa and further lowering the temperature to 520 °C, the Bi$_2$O$_2$Se nanosheets became smaller and brighter (Fig. 3a, right panel), indicating the attainment of thinner sheets. By controlling the CVD growth conditions, the precise and controllable manipulation of the thickness of 2D Bi$_2$O$_2$Se can be achieved, demonstrating a high level of accuracy and operability.
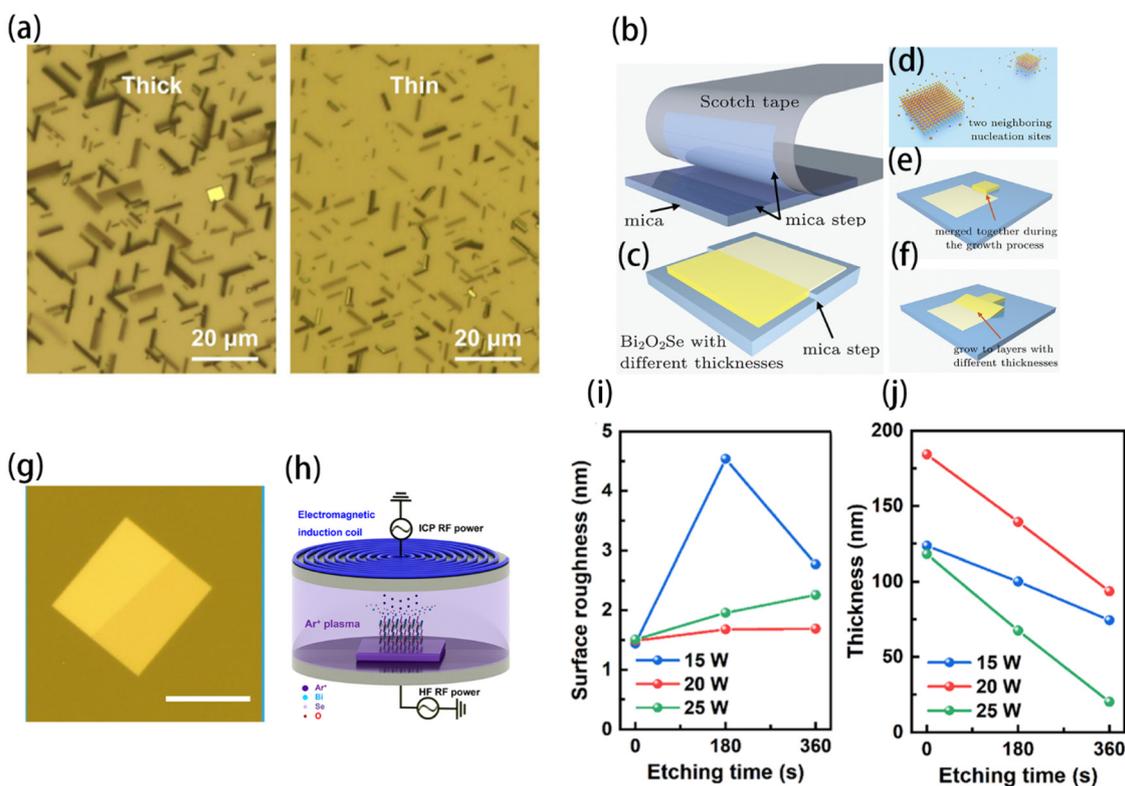
Fig. 3 Thickness modulation of Bi$_2$O$_2$Se. (a) OM images of as-grown Bi$_2$O$_2$Se nanosheets with different thicknesses. Reproduced with permission.[53] Copyright 2023, AIP Publishing. (b) Pre-treatment of the mica substrate with Scotch tape to form terraces. (c) Schematic of Bi$_2$O$_2$Se grown on the prepared substrate *via* CVD to obtain different thicknesses. (d–f) Schematic of the merging of nucleation sites and the growth process. (g) Optical microscope images of Bi$_2$O$_2$Se in-plane junctions with two different thicknesses. (b–g) Reproduced with permission.[57] Copyright 2019, IOP Science. (h) Diagram of the production of Ar$^+$ plasma and the etching process of Bi$_2$O$_2$Se nanoflakes in an ICP-RIE system. (i and j) Surface roughness and thickness of etched Bi$_2$O$_2$Se as a function of etching time (blue, green, and red lines represent different power levels). (h–j) Reproduced with permission.[59] Copyright 2022, American Chemical Society.

Hong *et al.*[57] employed a method involving successive peeling of mica substrates using Scotch tape, resulting in the formation of terraces on the mica surface (Fig. 3b). Then, Bi_2O_2Se was grown on the prepared substrate *via* CVD to obtain Bi_2O_2Se 2D in-plane junctions (IPJs) (Fig. 3c). A schematic diagram of the growth process is shown in Fig. 3d–f, and an optical image of Bi_2O_2Se with different thicknesses is shown in Fig. 3g. Their approaches are straightforward and practical, ensuring precise and scalable thickness modulation.

Inspired by the plasma etching method employed in materials like MoS_2,[58] Gao *et al.*[59] utilized argon plasma treatment to reduce the thickness of Bi_2O_2Se. A schematic representation of the argon plasma etching process is depicted in Fig. 3h. When the kinetic energy of Ar^+ transitions exceeds the atomic and interlayer binding energy of Bi, O, and Se atoms, a physical etching process occurs. Subsequent tests assessed the impact of different power levels and etching durations on the crystal quality and Bi_2O_2Se thickness, as shown in Fig. 3i and j. This innovative approach provides precise control over Bi_2O_2Se thickness. However, this method may introduce some defects onto the surface of Bi_2O_2Se.

3.2. Stress

Pressure, as a thermodynamic parameter, serves as a powerful tool for tuning intrinsic material properties. Under pressure, numerous materials manifest novel characteristics.[60–62] Pressure can be applied to Bi_2O_2Se synthesized *via* a solid-state reaction in a vacuum quartz tube by using a diamond anvil.[63] Pereira *et al.*[55] conducted a comprehensive study on the electronic structure changes to Bi_2O_2Se under high pressure using both theoretical and experimental approaches. Their experiments confirmed the excellent pressure stability of Bi_2O_2Se, revealing no significant structural alterations even under pressures as high as 30 GPa. Furthermore, they observed a sudden change in the band gap occurring at 4 GPa, as illustrated in Fig. 4a. This transition was attributed to the shortening and hardening of Bi–Se bonds under pressure, leading to changes in the characteristics of the topmost valence bands. Tian *et al.*[64] investigated the conductivity variation of Bi_2O_2Se under pressure and employed density functional theory (DFT) calculations to reveal its electronic structure changes under pressure. The resistance variation curve of Bi_2O_2Se samples with pressure is depicted in Fig. 4b, exhibiting pressure-induced superconductivity, with a transition occurring at 27.2 GPa, corresponding to a transition temperature of 3.6 K. Computational results indicate that in the presence of Se defects in Bi_2O_2Se, a flat band emerges in the conduction band, gradually approaching the Fermi level with increasing pressure, as illustrated in Fig. 4c. This flat band may be attributed to the superconductivity in Bi_2O_2Se.[64]

As a powerful means of manipulating material properties, strain exerts unique effects on Bi_2O_2Se.[65,66] Huang *et al.*, based on DFT calculations, demonstrated the influence of uniaxial strain on the bulk electronic structure of Bi_2O_2Se, including a transition from an indirect band gap to a direct band gap under 1.5% out-of-plane compressive strain (Fig. 4d).[65]

Furthermore, the light-harvesting performance of bulk Bi_2O_2Se was investigated along the *a* and *c* directions. Under unstrained conditions, both *αα* and *αc* exhibit distinct absorptions ranging from the violet to the ultraviolet region. However, with a compressive strain of 1.5% applied along the *c*-axis, the absorption spectrum is initiated in the near-infrared region and extends to the ultraviolet region, accompanied by a redshift in the absorption edge (Fig. 4e).

3.3. Defect engineering

Defects in Bi_2O_2Se exert a significant influence on its electrical properties, particularly, conductivity.[64] Additionally, studies suggest that vacancies within the sublattice of 2D Bi_2O_2Se have a pronounced impact on its optical absorption and thermal characteristics.[68–70] Gao *et al.* and Ni *et al.* utilized Ar^+ plasma treatment to manipulate defect states in 2D Bi_2O_2Se. This treatment increased the number of oxygen and selenium vacancies in the Bi_2O_2Se nanosheets, significantly enhancing the capture and recombination rates of photogenerated carriers.[59,68] Yang *et al.*[71] synthesized nonstoichiometric Bi_2O_xSe ($x < 2$) flakes by CVD at low temperature. The resulting material exhibited significantly lower thermal conductivity at room temperature compared to stoichiometric Bi_2O_2Se, decreasing from 1.2–1.9 $W\ m^{-1}\ K^{-1}$ to $0.68 \pm 0.06\ W\ m^{-1}\ K^{-1}$, which was nearly three times lower. Meanwhile, understanding the intrinsic point defects and accurately characterizing these defects in Bi_2O_2Se is also crucial for further studies. The concentration of defects in Bi_2O_2Se is predominantly influenced by the energy associated with defect formation. As a ternary compound with a distinctive layered structure, Bi_2O_2Se contains a substantial amount of defects.[54] Li *et al.*[54] extensively examined the native point defects in Bi_2O_2Se through first-principles methods. This included the investigation of vacancies, interstitials, and antisites in their respective charge states. They calculated the formation energies of various defects under Se-poor, Bi-rich, Se-rich, and Bi-poor conditions, as depicted in Fig. 4f. Their findings indicate that Se vacancies (Se_v) and oxygen vacancies (O_v) are the predominant defects; this agrees well with previous reports.[24] The visualization of crystal defects is equally crucial, especially for CVD-grown Bi_2O_2Se. It enables the assessment of the quality of the nanosheets grown. Some non-destructive studies on defects in graphene have been conducted using Raman spectroscopy.[72,73] Kim *et al.*[67] conducted a study involving CVD-grown individual square Bi_2O_2Se nanosheets. By increasing the flow rate of Ar gas, aggregated Bi_2O_2Se polygons were obtained, exhibiting a higher density of defects due to the rapid growth process. The Raman scattering process and spectra were comprehensively analyzed under both excitation modes. Their results revealed oscillations at $\sim 55\ cm^{-1}$ associated with line defects in the crystal. They also observed the presence of grain boundaries under excitation at 785 nm (Fig. 4g). However, more detailed investigations into defects in Bi_2O_2Se are still expected. This includes, for example, *in situ* observations of Bi_2O_2Se under electron beam irradiation using TEM, as well as the study of predominant defects in 2D Bi_2O_2Se synthesized *via* various methods.
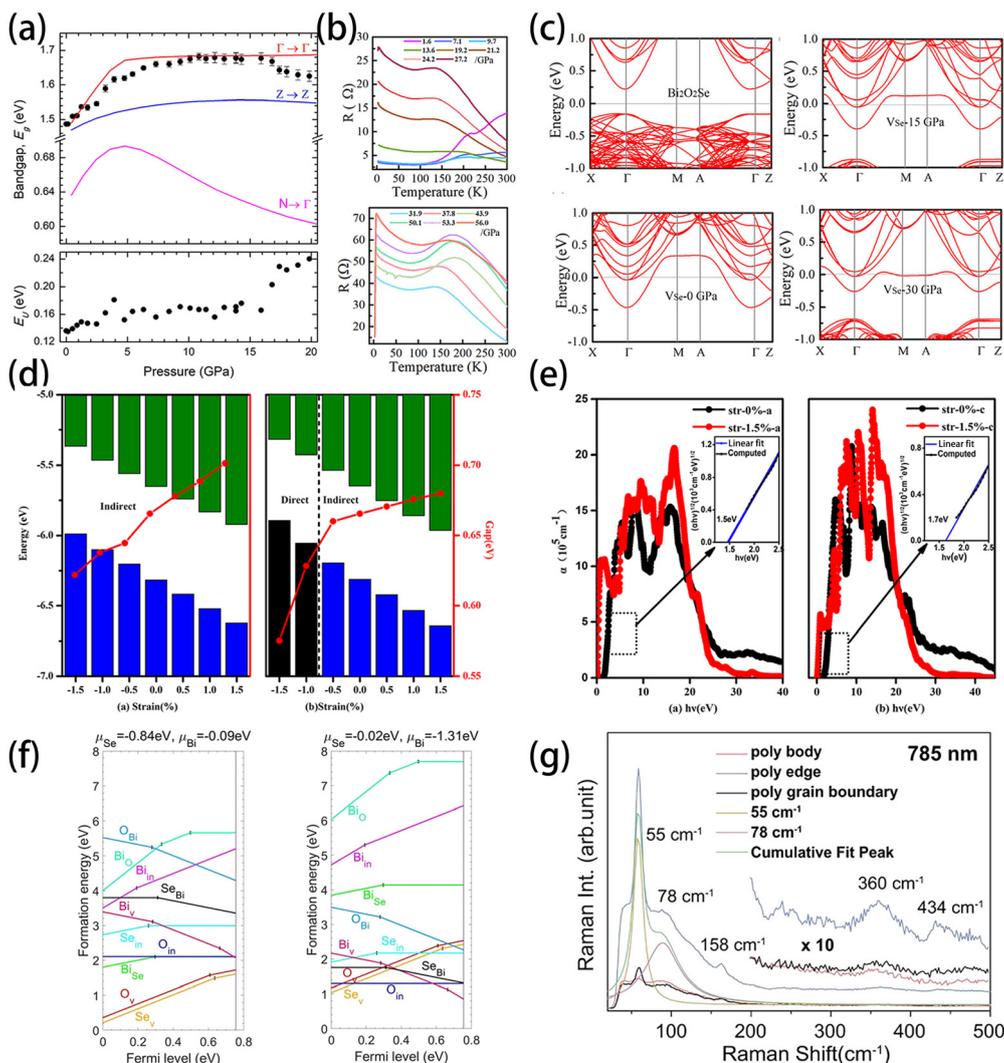
Fig. 4 Influence of stress and defects on the properties of Bi_2O_2Se. (a) Pressure-induced band-gap variations in Bi_2O_2Se, with experimental data (dots), calculated trends for direct $\Gamma-\Gamma$ (red) and $Z-Z$ (blue) transitions, and theoretical $N-\Gamma$ indirect band gap (pink); pressure-dependent Urbach energy changes in Bi_2O_2Se (bottom). Reproduced with permission.[55] Copyright 2018, American Chemical Society. (b) Resistance of Bi_2O_2Se samples under pressures from 1.6 to 56 GPa. (c) Band structure of Bi_2O_2Se, including Se vacancy effects and flat band shifts under increasing pressure. (b and c) Reproduced with permission.[64] Copyright 2024, American Chemical Society. (d) Electronic band structure of bulk Bi_2O_2Se under unstrained conditions and along the c-axis with a compressive strain of 1.5%. (e) Calculated absorption coefficients αa and αc of bulk Bi_2O_2Se for the unstrained state (black line with filled circles) and the strained state (red line with filled circles). Inset shows the magnified optical band gap fitted from the absorption edge. (d and e) Reproduced with permission.[65] Copyright 2019, AIP Publishing. (f) Defect formation energies as a function of Fermi level, Se-poor, Bi-rich conditions (left panel); Se-rich, Bi-poor conditions (right panel). Reproduced with permission.[54] Copyright 2018, Springer Nature. (g) Raman spectra of Bi_2O_2Se under 785 nm excitation and grain boundaries can be found. Reproduced with permission.[67] Copyright 2022, American Chemical Society.

4. Synthesis methods

In the realm of cutting-edge electronics and optics, high demands are placed on material size, thickness, and crystallinity. Therefore, it is of paramount importance to explore methods for obtaining high-quality and crystalline Bi_2O_2Se. Researchers have proposed various synthesis strategies to cater to different practical applications. These methods include mechanical exfoliation,[74–76] MBE,[29] CVD[24,25,28,77] and PLD[78]. In addition, materials obtained from different synthesis methods may have differences in structure and properties, so it is necessary to comprehensively compare and evaluate them. In this section, we review a series of methods for preparing 2D Bi_2O_2Se and their influences on its properties.

When it comes to the growth of 2D materials, selecting an appropriate substrate stands out as a significant step.[79,80] Bi_2O_2Se has a unique layered structure and strong bonding properties, as well as pronounced out-of-plane electrostatic interactions. These properties enable the preparation of ultra-thin Bi_2O_2Se layers during vapor deposition progress. In par-

ticular, mica is an ideal substrate for Bi_2O_2Se growth because it is chemically inert and has relatively weak interactions with Bi_2O_2Se. This enables precise control over the nucleation and growth processes,[24,31] resulting in the self-organized growth of Bi_2O_2Se along the [001] crystal axis of mica (Fig. 5a, confirmed by X-ray diffraction (XRD)).

However, Bi_2O_2Se has a lattice mismatch with the [001] surface of mica,[79] which leads to the random orientation of the synthesized Bi_2O_2Se crystals in the in-plane direction. And researchers found that the cubic perovskite $SrTiO_3$ ($a = b = 3.905$ Å) had perfect lattice matching with Bi_2O_2Se (Fig. 5b, confirmed by HAADF-STEM). This provides a good platform for the growth of high-quality and large-area Bi_2O_2Se films.[29,77]

4.1. Exfoliation

Due to the predominant vdW interactions between layers in most 2D materials, resulting in relatively weak interlayer bonding, exfoliation has become the most prevalent method for obtaining such materials. However, as previously stated, due to the strong interlayer forces within Bi_2O_2Se, mechanical exfoliation poses a significant challenge.[24,38] Therefore, research regarding mechanical exfoliation remains an area yet to be thoroughly investigated. Research by Pan *et al.* on the shear exfoliation of Bi_2O_2Se is highly influential,[74–76] leading to significant advances in the field. Their extensive series of experiments culminated in the development of a novel and convenient method using a kitchen blender to produce large-scale Bi_2O_2Se nanosheets (Fig. 5c).[74] These shear-exfoliated

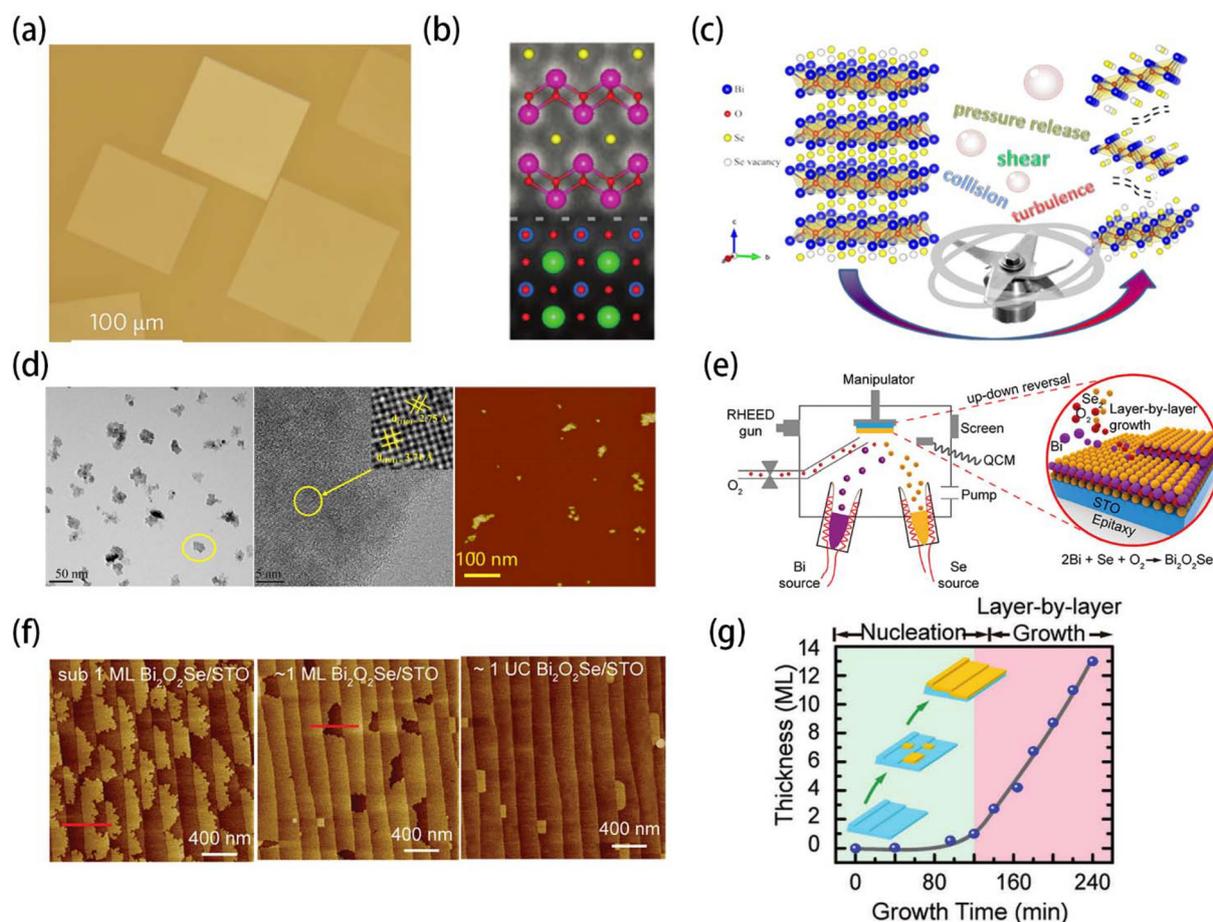**Fig. 5** Synthesis methods (exfoliation and MBE). (a) OM image of Bi_2O_2Se nanosheets grown on mica shows a random distribution. Reproduced with permission.[24] Copyright 2017, Springer Nature. (b) HAADF-STEM image of Bi_2O_2Se (~10 nm) at the interface with STO [001] shows a clear interface between the Bi_2O_2Se nanosheets and the STO lattice. Reproduced with permission.[29] Copyright 2019, Wiley. (c) Process of shear exfoliation in Bi_2O_2Se achieved through the utilization of a common kitchen blender. Reproduced with permission.[74] Copyright 2019, American Chemical Society. (d) TEM (left panel), HR-TEM (middle panel), and AFM (right panel) images of 2D Bi_2O_2Se obtained through a combined approach of lithium intercalation and liquid-phase shear exfoliation. Reproduced with permission.[81] Copyright 2019, American Chemical Society. (e) Schematic of MBE equipment and the growth process. (f) AFM images of Bi_2O_2Se on STO in its growth process (left panel). In the process of MBE growth, irregularly shaped 2D islands of Bi_2O_2Se form at the steps of the $SrTiO_3$ substrate (middle panel). Monolayer (ML) Bi_2O_2Se film (right panel) grown to ~1 UC (2 ML) forms new 2D islands at the steps of the substrate, with more regular morphologies. (g) Function describing the variation of thickness with growth time: nucleation process occurs approximately within the first 100 min, followed by a growth process. (b and e–g) Reproduced with permission.[29] Copyright 2019, Wiley.

nanosheets exhibited an average thickness of 20–30 layers. Subsequent research demonstrated that shear exfoliation facilitated the introduction of Se vacancies, which enhanced the thermoelectric performance of Bi_2O_2Se. Huang *et al.*[81] achieved the exfoliation of Bi_2O_2Se through a combination of lithium intercalation and assisted shear forces (Fig. 5d). However, to date, none of the exfoliation methods can yield well-defined 2D Bi_2O_2Se with a suitable morphology for the study of optoelectronic properties. More advanced exfoliation and synthesis methods are still needed for further investigation.

4.2. Molecular beam epitaxy (MBE)

MBE is a method of epitaxial film deposition, and it is also a special vacuum deposition process. This method involves the sequential layer-by-layer growth of thin films along the crystal axis of the substrate, under specific substrate conditions.[82] Liang *et al.*[29] first obtained a single-layer Bi_2O_2Se film using MBE by optimizing the flow rates and temperatures of the components. The growth progress is shown in Fig. 5e. A two-dimensional growth pattern of Bi_2O_2Se on a $SrTiO_3$ substrate was realized through the co-evaporation of Bi and Se precursors in the presence of oxygen. The crucial factors for achieving MBE growth of Bi_2O_2Se atomic thin films include an appropriate substrate growth temperature (T_s), Se/Bi flow ratio, and oxygen pressure within the molecular beam epitaxy system. A conventional three-temperature method was employed, with temperatures set to $T_{Bi} > T_s > T_{Se}$.[83] By optimizing the parameters, they controlled the flux rates of Se and Bi to be 7 and 3 Å min^{-1}, respectively. They obtained a single-layer Bi_2O_2Se film at $T_s = 290$ °C and an oxygen pressure of 1×10^{-4} mbar. In the initial stages of growth, single-layer Bi_2O_2Se islands preferentially nucleate along the steps of the $SrTiO_3$ substrate. These islands exhibit irregular edges and form discontinuous 2D structures (Fig. 5f, left panel). As growth progresses and coverage increases, these isolated single-layer islands begin to coalesce. This results in the formation of continuous monolayer films that cover the entire surface of the STO (001) substrate. Remarkably, these films strictly conform to the underlying step structure (Fig. 5f, middle panel). When they further increased the growth coverage, the two-dimensional islands on the Bi_2O_2Se layer had regular edges that were parallel to each other, as shown in Fig. 5f, right panel. They also summarized the film thickness as a function of growth time (Fig. 5g). Their results showed that the homoepitaxial growth of Bi_2O_2Se was more favorable than heteroepitaxial growth on $SrTiO_3$ substrates. Given the high operational costs of MBE, research on the growth of 2D Bi_2O_2Se materials using MBE is notably scarce. Consequently, further experimental studies are required to optimize parameters such as evaporation temperature and gas flow rate within the MBE process.

4.3. Chemical vapor deposition (CVD)

CVD is a method for epitaxially depositing solid material films on a substrate surface in a controlled chemical reaction gas phase. CVD offers high controllability over the morphology and crystallinity of synthesized products, making it a widely employed technique for the preparation of large-area, high-crystallinity 2D materials.[84,85] The key processes of CVD can be succinctly summarized by the following three steps: the first step is the decomposition of the precursor materials, in which the gaseous precursor materials are heated to their decomposition temperature to decompose into reaction species such as atoms, molecules, or ions. The second step is transport and reaction, in which the decomposition products are transported in the gas phase to the substrate surface and undergo a chemical reaction on the substrate surface. The last step is the formation of the solid deposition.[86] Due to its distinct layered configuration, Bi_2O_2Se tends to crystallize predominantly as extremely thin 2D crystals with significant lateral dimensions on a compatible substrate during the CVD growth process.[24] Currently, most of the research on Bi_2O_2Se is based on CVD to obtain high-quality samples.

Wu *et al.*[24] first synthesized Bi_2O_2Se on a mica substrate using Bi_2O_3 and Bi_2Se_3 as precursors and argon as the carrier gas. A schematic is given in Fig. 6a.[25] Subsequently, numerous studies have been conducted on the CVD synthesis of Bi_2O_2Se. Khan *et al.*[26] conducted thermogravimetric analysis on Bi_2Se_3 over a temperature range from room temperature to 1000 °C. They observed that the incorporation of salt could lower the melting point of Bi_2Se_3,[87] leading to the proposal of a salt-assisted CVD method for synthesizing high-quality 2D Bi_2O_2Se at a low temperature of 500 °C, as depicted in Fig. 6b. Their approach exhibits distinct advantages for enabling low-temperature synthesis. Inspired by previous synthesis methods for MoS_2,[37,88] Tong *et al.*[28] refined the CVD growth technique, employing a face-down growth mode. This approach, illustrated in Fig. 6c, led to the attainment of Bi_2O_2Se nanosheets with larger domain sizes of approximately 180 μm (Fig. 6d) and a thickness of ~10 nm (Fig. 6e), indicative of high-quality material. They assumed that during the growth process, Bi_2O_3 in the vapor phase could potentially form an intermediate phase, Bi_2O_{3-x}, which then diffused to the mica surface. Subsequently, it further reacted with Bi_2Se_3 to yield Bi_2O_2Se.

Fu *et al.*[25] proposed a universal non-corrosive method for transferring CVD-grown Bi_2O_2Se. They developed a polystyrene (PS)-assisted transfer method (Fig. 6f), which involved first coating the f-mica surface with PS, followed by a 15 min bake at 80 °C to ensure adhesion. Subsequently, a further 15 min curing at 80 °C was conducted. Then, aided by deionized (DI) water, the PS film was peeled off together with Bi_2O_2Se from the f-mica substrate. The PS film was then transferred onto a silicon substrate, baked for 1 h at 70 °C, and finally cleaned with toluene to obtain the final Bi_2O_2Se sample. However, due to the strong electrostatic interactions between 2D Bi_2O_2Se and the substrate, transferring Bi_2O_2Se is more challenging and material damage is easier compared to other 2D materials.[89,90] To minimize damage during the transfer process and optimize device performance, several growth strategies have been proposed. These include seed-induced vertical growth,[91] inclined growth,[92] horizontally self-standing growth[93] and transfer-free growth.[94] Zhu *et al.*[91] substantiated the seed-induced growth
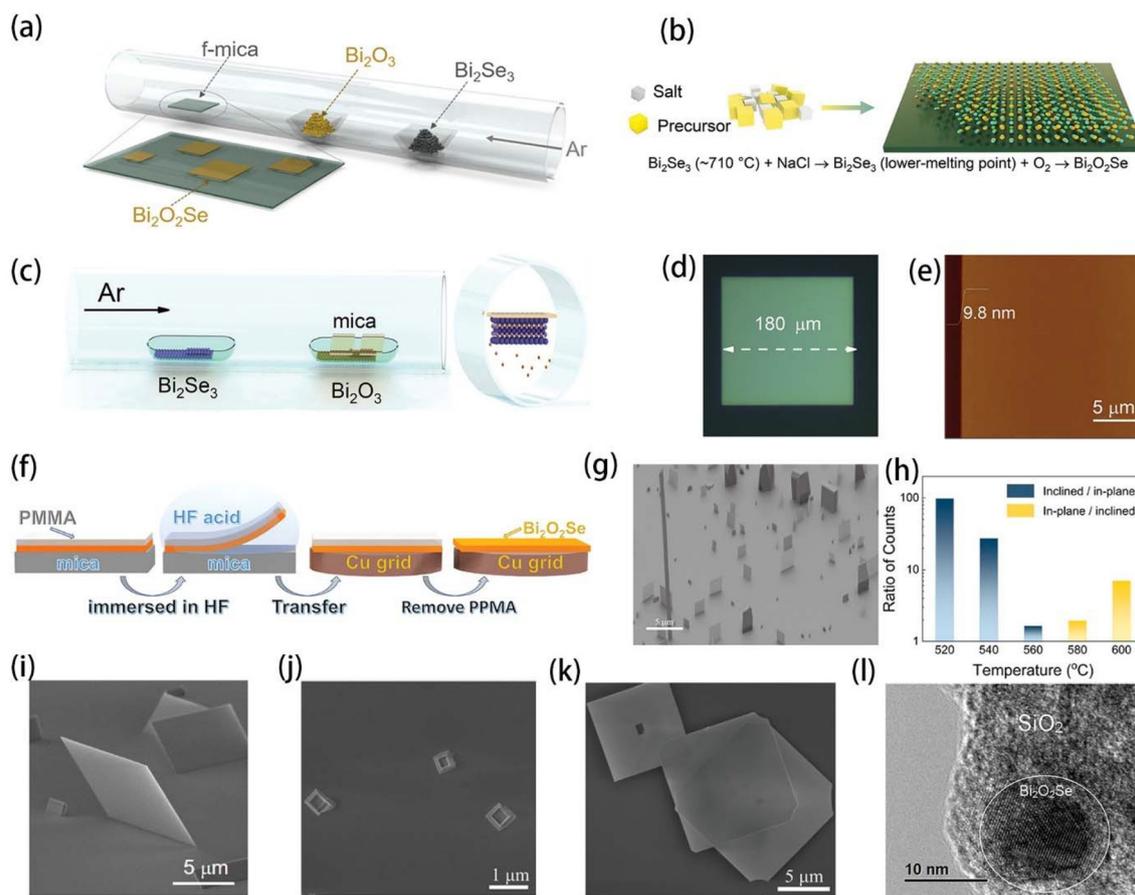
Fig. 6 CVD growth of Bi_2O_2Se on mica and transfer methods. (a) Schematic illustration of Bi_2O_2Se growth *via* CVD using Bi_2O_3 and Bi_2Se_3 as precursors. (b) Schematic of large-scale growth of salt-assisted 2D Bi_2O_2Se nanosheets at a low temperature of 500 °C. Reproduced with permission.[26] Copyright 2022, Wiley. (c) Illustration of the optimized CVD method in face-down growth mode. (d) Optical microscope image of the synthesized Bi_2O_2Se nanosheets exhibiting domain sizes of approximately 180 μm. (e) AFM image of the as-grown Bi_2O_2Se nanosheets reveals a thickness of approximately 9.8 nm. (c–e) Reproduced with permission.[28] Copyright 2019, Wiley. (f) Schematic of the PS-assisted transfer method of Bi_2O_2Se nanosheets. (a and f) Reproduced with permission.[25] Copyright 2019, Wiley. (g) SEM image of vertically grown Bi_2O_2Se nanosheets with seed layers. Reproduced with permission.[91] Copyright 2019, Wiley. (h) Ratio of sample counts between in-plane growth and inclined growth. (i) SEM image of as-grown inclined Bi_2O_2Se on mica. (h and i) Reproduced with permission.[92] Copyright 2020, American Chemical Society. (j) SEM image of 3D islands grown under high pressure. (k) SEM image of horizontally self-standing Bi_2O_2Se synthesized by the two-step method. (j and k) Reproduced with permission.[93] Copyright 2022, Wiley. (l) HR-TEM image of a circular Bi_2O_2Se sample formed on the SiO_2 surface. Reproduced with permission.[94] Copyright 2020, Wiley.

of 2D Bi_2O_2Se through DFT calculations and experimental verification. They observed that Bi_2O_3 could act as a seed to influence the growth orientation of Bi_2O_2Se. Their research results indicated that there was an appropriate binding energy between the (111) crystal plane of Bi_2O_3 and the (001) crystal plane of mica. Additionally, there is a relatively high lattice match between Bi_2O_3-(111) and Bi_2O_2Se-(100), resulting in the preferential growth of Bi_2O_2Se oriented perpendicular to the (100) direction of the Bi_2O_3 layer. Subsequently, they conducted growth experiments on Bi_2O_2Se using different atomic ratios of Bi_2O_3 to Bi_2Se_3, specifically 2 : 1 and 2.5 : 1. They observed significant changes in the growth mode with varying Bi_2O_3 content. When the atomic ratio was 2 : 1, a planar growth mode was observed, while an excess of Bi_2O_3 induced the vertical growth of Bi_2O_2Se nanosheets (Fig. 6g). In this way, due to the minimized interaction with mica brought about by

vertical growth, the transfer of Bi_2O_2Se nanosheets was easier, enabling convenient transfer using a tungsten probe. However, a transition region between Bi_2O_3 and Bi_2O_2Se forms at the base of Bi_2O_2Se, where grain boundary scattering is inevitable.[95] So Hong *et al.*[92] addressed this challenge by designing an inclined growth mode for 2D Bi_2O_2Se without the use of seeding layers. By carefully adjusting the CVD growth conditions, they demonstrated how the ratio of inclined to in-plane growth modes varied with temperature, as shown in Fig. 6h. Their results indicate that inclined growth effectively reduces the unneutralized charge density at the Bi_2O_2Se/mica interface. At lower temperatures, precursor clusters on the mica surface have limited diffusion distances, which suppress in-plane growth. A SEM image of the as-grown inclined Bi_2O_2Se is shown in Fig. 6i. Using this growth method, Bi_2O_2Se can be easily separated from the substrate with a light press.

Wang et al.[93] achieved horizontally self-standing Bi_2O_2Se nanoplates by applying abrupt pressure changes to switch between kinetic and thermodynamic growth processes. Under an initial high pressure of 25 kPa, Bi_2O_2Se crystals exhibited 3D island growth (Fig. 6j), primarily governed by kinetic processes. The pressure was then reduced to 50 Pa within 30 s, promoting both molecular diffusion and precursor evaporation. This overcame the kinetic barriers to 2D growth, transitioning the process to a thermodynamic regime. Additionally, the unsaturated dangling bonds at the edges of the 3D islands facilitated the lateral growth of Bi_2O_2Se. The SEM image of the product is shown in Fig. 6k. Sagar et al.[94] developed a transfer-free method for growing Bi_2O_2Se on SiO_2 substrate. They utilized

Bi_2Se_3 as the single precursor, with silicon dioxide (SiO_2) serving as both the substrate and oxygen source for Bi_2O_2Se synthesis. Circular Bi_2O_2Se with a thickness of 5–10 nm was obtained on the SiO_2 surface, as depicted in Fig. 6l.

As mentioned earlier, due to the good lattice matching between Bi_2O_2Se and the perovskite oxides,[29,77] there have been studies opting for $SrTiO_3$ as the substrate for growing Bi_2O_2Se in order to attain a more perfect morphology. Tan et al.[96] successfully grew single-crystal Bi_2O_2Se films on the conventional perovskite oxides, including $SrTiO_3$(STO), $LaAlO_3$ (LAO), and LSAT. Characterization studies using HAADF-STEM and ABF-STEM revealed a well-defined interface between Bi_2O_2Se and $SrTiO_3$ on the substrate, as demonstrated in
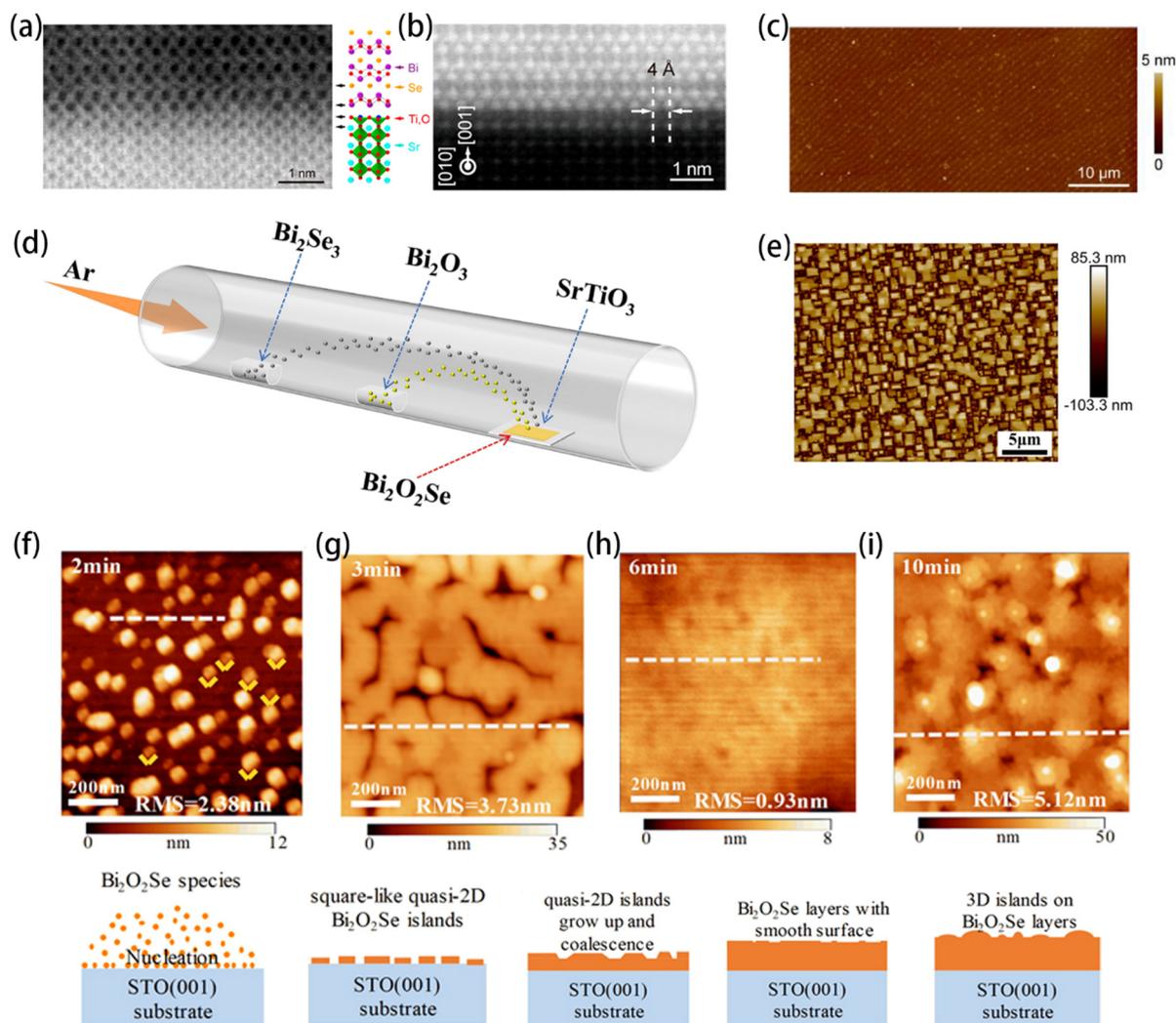
Fig. 7 CVD and PLD growth of Bi_2O_2Se on $SrTiO_3$(STO) substrate. ABF-STEM image (a) and HAADF-STEM image with atomic resolution (b), demonstrating a clear interface between the Bi_2O_2Se thin film and the substrate (STO). (c) AFM image of a large-area quasi-monolayer Bi_2O_2Se thin film with a smooth surface and second-layer islands on the continuous monolayer. (a–c) Reproduced with permission.[96] Copyright 2019, American Chemical Society. (d) Schematic of Bi_2O_2Se growth on $SrTiO_3$ substrate via CVD. (e) AFM image of the Bi_2O_2Se thin film displays a multitude of single-crystal domains composing the film. (d and e) Reproduced with permission.[77] Copyright 2023, Elsevier. (f–i) AFM images of the Bi_2O_2Se surface morphology at different deposition times: (f) nucleation process, (g) formation of quasi-2D Bi_2O_2Se islands, (h) quasi-2D growth process at 6 min deposition time showing a smooth surface, and (i) increased deposition time of 10 min resulting in a relatively rougher surface. (f–i) Reproduced with permission.[78] Copyright 2020, IOP Publishing.

Table 1 Summary of the growth conditions, substrates, precursors, and resulting sample thickness required for the synthesis of 2D Bi_2O_2Se

Synthesis method	Material type	Substrate	Precursors	Growth conditions	Thickness
MBE[29]	2D film	STO	Bi, Se, O_2	T_s = 290 °C, 10^{-4} mbar	Monolayer–1 UC
Exfoliation[74]	2D flake	N/A	Bi_2O_2Se	N/A	20–30 layers
Exfoliation[81]	2D flake	N/A	Bi_2O_2Se	N/A	2.8 nm
CVD[31]	2D flake	Mica	Bi_2O_3, Bi_2Se_3	650–700 °C, 50–100 sccm Ar	7.7 nm
CVD[25]	2D flake	Transferred to Si	Bi_2O_3, Bi_2Se_3	350–400 Torr, 620 °C, 170 sccm Ar	5.2 nm
CVD[28]	2D flake	Mica	Bi_2O_3, Bi_2Se_3	550–630 °C, 100–150 sccm Ar	9.8 nm
CVD[26]	2D flake	Mica	Bi_2Se_3, O_2	100 sccm O_2 and 190 sccm Ar	1.3–11 nm
CVD[94]	Crystal	SiO_2	Bi_2Se_3, SiO_2	750 °C	5 nm
CVD[96]	2D film	STO	Bi_2O_3, Bi_2Se_3	660–675 °C, 300 Torr, 200 sccm Ar	Few layer–30 nm
CVD[96]	2D film	LAST	Bi_2O_3, Bi_2Se_3	660–675 °C, 300 Torr, 200 sccm Ar	Few layer–30 nm
CVD[96]	2D film	LAO	Bi_2O_3, Bi_2Se_3	660–675 °C, 300 Torr, 200 sccm Ar	Few layer–30 nm
CVD[77]	2D film	STO	Bi_2O_3, Bi_2Se_3	120 Pa, 600 °C, 123 sccm Ar	N/A
PLD[78]	2D film	STO	Bi_2O_3, Bi, Se	10^{-5} Pa, 425–500 °C	27–83 nm

Fig. 7a and b. Furthermore, they achieved monolayer thickness by reducing precursor supersaturation through employing lower growth temperatures and higher system pressures. The resulting Bi_2O_2Se films exhibited a smooth planar morphology, as illustrated in Fig. 7c. This approach guarantees the high-quality growth of Bi_2O_2Se films and the attainment of the desired film thickness. Ren *et al.*[77] successfully synthesized large-area Bi_2O_2Se thin films on $SrTiO_3$ substrates with dimensions of 2 cm by 2 cm and a thickness of 100 nm using the CVD method (Fig. 7d). The film is composed of numerous Bi_2O_2Se nanosheets with a well-defined atomic arrangement, as observed in Fig. 7e. This structural configuration provides a solid foundation for the long-term stable operation of photodetectors, endowing them with excellent performance and broadband response characteristics.

In summary, although significant progress has been made in the growth of Bi_2O_2Se films using the CVD method, achieving large-scale production still requires further research and technological innovation. Through continuous optimization of synthesis techniques, the exploration of novel preparation methodologies, and the introduction of automated production equipment, we anticipate overcoming the current preparation challenges, ultimately enabling the large-scale production of 2D Bi_2O_2Se materials.

4.4. Pulsed laser deposition (PLD)

PLD is a representative physical vapor deposition technique that has been successfully employed in the synthesis of various two-dimensional materials such as graphene,[97] MoS_2,[98] WS_2,[99] and BN.[100] This method has been demonstrated to serve as an alternative to CVD. Song *et al.*[78] first employed PLD to synthesize Bi_2O_2Se on STO substrates. The process involves three main steps: firstly, a high-density Bi_2O_2Se polycrystalline target was obtained using a dual-phase solid-state reaction approach with starting materials of Bi_2O_3 (4 N), Se (4 N), and Bi (4 N). The second step involved pulsed laser irradiation, causing a portion of the Bi_2O_2Se target to evaporate or ionize into a plasma. This plasma diffused from the target to the substrate, resulting in the formation of 2D Bi_2O_2Se films. AFM images in Fig. 7f–i illustrate the growth process. The results indicate a transition in the growth mode

of Bi_2O_2Se on STO substrates from quasi-2D layered structures to 3D island structures. The figures show that the formation of 3D island-like structures leads to a higher surface roughness of approximately 5.12 nm.

Conversely, reducing the deposition time to 6 min significantly decreases the surface roughness to only ~0.93 nm. PLD has a growth rate approximately 10 times faster than the CVD method.[96] This relatively fast growth rate provides a good foundation for the efficient production of Bi_2O_2Se devices in the future. Therefore, strict control of the growth conditions is crucial for achieving smooth films. With ongoing advancements in PLD technology, its application in the growth of two-dimensional materials is anticipated to extend to even more diverse fields. Table 1 comprehensively summarizes the synthesis conditions of 2D Bi_2O_2Se and the resulting dimensions of the products, indicating that, apart from exfoliation, all synthesis processes are conducted under low-pressure conditions.

5. Applications for 2D Bi_2O_2Se

2D Bi_2O_2Se has become widely recognized for its impressive electronic properties and robust air stability in numerous scientific fields. Its distinctive two-dimensional architecture imparts exceptional performance, paving the way for widespread applications in electronics, optoelectronics, and other related fields. This section provides a comprehensive overview of the specific applications of Bi_2O_2Se in various functional devices, encompassing FETs,[24,52,101] photodetectors,[28,90,102–105] neuromorphic computing and optoelectronic synapses.[106–110]

5.1. FETs

FETs, serving as the cornerstone of modern integrated circuits, facilitate the realization of highly intricate electronic functionalities by integrating a multitude of FETs on a single chip, thereby propelling the rapid advancement of information technology. Recently, the exploration of electronic devices with higher performance and smaller dimensions has become imperative. 2D Bi_2O_2Se emerges as a robust choice for FETs, owing to its outstanding electron mobility and the superior gate dielectric characteristics inherent in 2D materials. Peng

et al.[24] first reported the application of 2D Bi_2O_2Se in FETs, demonstrating outstanding performance. They achieved a maximum Hall mobility of 29 000 cm^2 V^{-1} s^{-1} at 1.9 K and 450 cm^2 V^{-1} s^{-1} at room temperature. Additionally, the device exhibited a remarkable on/off ratio of up to 10^6 and a subthreshold swing value close to the ideal of 65 mV dec^{-1} at room temperature. Importantly, these performance characteristics indicate the potential for further optimization. Building upon this research, Yang and coworkers[52,101] conducted simulations on the performance limits of monolayer and bilayer Bi_2O_2Se FETs. Their predictive outcomes indicate that optimized bilayer Bi_2O_2Se FETs have the potential to meet the requirements for high-performance transistors according to the International Technology Roadmap for Semiconductors (ITRS) when the gate length is reduced to 5 nm. For monolayer Bi_2O_2Se FETs, achieving *n*-type and *p*-type channel lengths of 2 nm and 3 nm, respectively, is necessary. These results offer a new avenue for extending Moore's law to the 2–3 nm scale. A breakthrough was made for Bi_2O_2Se-based Fin FETs.[23] In this study, high-*k* dielectrics Bi_2SeO_5 and 7 nm thick HfO_2 are deposited on the vertically aligned 2D Bi_2O_2Se surface.[111] A 2D Fin FET with a channel length of 400 nm was fabricated, exhibiting excellent electrostatic control. Under a V_{DS} of 2 V and a V_G of 3 V, the device demonstrated an off-state current density (I_{OFF}) of less than 0.1 nA μm^{-1}, an on/off current ratio (I_{ON}/I_{OFF}) greater than 10^7, and a relatively high on-state current density of up to 830 μA μm^{-1}. Cheng's team[27] introduced a self-limiting vapor–solid (VS) deposition technique for synthesizing atomically thin 2D Bi_2O_2Se and subsequently fabricated phototransistors based on Bi_2O_2Se FETs. Exhibiting a remarkable on/off ratio of ~10^9, a responsiveness of 2.2×10^4 A W^{-1}, and a detection rate of 3.4×10^{15} Jones, these results represent the highest performance among 2D materials, including Bi_2O_2Se. Elevating the crystal quality of 2D Bi_2O_2Se is a pivotal determinant for its large-scale applications. It necessitates more precise control of the synthesis process to enhance crystal quality, coupled with more advanced encapsulation techniques. These aspects warrant further in-depth research in the future. Besides this, improving electrode contact is another way to optimize the performance of FETs, influencing aspects such as current transmission, switching speed, and power consumption. Liu and Xu *et al.*[112,113] conducted quantum transport simulations through first-principles calculations on the contacts between single-layer and bilayer Bi_2O_2Se and 6 types of commonly used metal electrodes (Sc, Ti, Ag, Au, Pd, and Pt). The results reveal that due to the Fermi level pinning (FLP) effect at the interface, single-layer Bi_2O_2Se forms well-established *n*-type ohmic contacts with Pt, Sc, and Ti, while bilayer Bi_2O_2Se forms *n*-type ohmic contacts with all six metals. This finding further corroborates the potential applications of Bi_2O_2Se in constructing high-performance FETs and underscores the crucial role of Fermi level pinning in regulating the contact properties between the material and metal electrodes. However, experimental evidence in this regard is somewhat lacking, and future experiments are eagerly anticipated to validate the simulation results and provide a comprehensive understanding of the actual contact behavior between Bi_2O_2Se and metal electrodes.

5.2. Photodetectors

Photodetectors are pivotal in the transformation of optical signals into electrical signals, enabling the detection and measurement of parameters such as light intensity and wavelength in the surrounding environment. The exceptional electron mobility and strong light–matter interactions of 2D Bi_2O_2Se make it an ideal optoelectronic material. Therefore, advancing the development of Bi_2O_2Se photodetectors facilitates efficient detection and conversion of optical signals, providing high-performance optoelectronic sensors for diverse applications.

Bi_2O_2Se detectors exhibit high responsivity across visible and infrared wavelengths,[102] with the capability to extend into the THz range.[105] These properties enable applications in efficient broad-spectrum detection and full-color imaging.[103] Peng *et al.*[102] pioneered a wet-chemical etching method, utilizing a mixed solution of H_2SO_4 and H_2O_2 to pattern CVD-grown 2D Bi_2O_2Se. Testing different solution ratios determined that the optimal volume ratio was $H_2SO_4 : H_2O_2 : H_2O = 2 : 4 : 8$. The etching process (Fig. 8a) demonstrated that even after etching, the Bi_2O_2Se array maintained an outstanding charge carrier mobility of up to 209 cm^2 V^{-1} s^{-1} at 300 K. Simultaneously, the patterned Bi_2O_2Se array (Fig. 8b) exhibited a significantly high photoresponsivity at a wavelength of 532 nm, reaching 2000 A W^{-1}, confirming that the impact of etching on the material quality of Bi_2O_2Se could be disregarded. Yin *et al.*[90] also reported a high-speed infrared photodetector based on Bi_2O_2Se, exhibiting a responsivity of 65 A W^{-1} and an ultrafast response time of ~1 ps. Simultaneously, the device displayed outstanding flexibility (up to 1% strain) and excellent air stability, as illustrated in Fig. 8c and d. Their research contributes significantly to the development of low-cost, highly sensitive infrared detectors. Chen *et al.*,[105] through the antenna-assisted metal–semiconductor–metal (MSM) structure (Fig. 8e), successfully extended the detection range of the Bi_2O_2Se photodetector from the infrared to the terahertz (THz) region and applied it to imaging, as depicted in Fig. 8f–i. It is noteworthy that terahertz waves can penetrate plastic but are strongly absorbed by water. This study provides a theoretical and experimental foundation for the application of terahertz waves in detecting illicit substances and conducting health screenings. Wang *et al.*[103] reported the application of Bi_2O_2Se nanosheets in full-color imaging. The photodetector based on these nanosheets achieved a high responsivity of 523 A W^{-1} and a detection rate of 1.37×10^{11} Jones under irradiation with a laser power density of 102 mW cm^{-2} and a wavelength of 400 nm. Also, utilizing a non-cryogenic pixel scanning system (Fig. 8j), the successful realization of high-quality full-color imaging for the detector was accomplished. Tong *et al.*,[28] through an improved CVD growth method (as mentioned earlier), successfully fabricated a high-performance Bi_2O_2Se phototransistor, achieving an impressive responsivity of 108 696 A W^{-1} at a wavelength of 360 nm. Their research high-
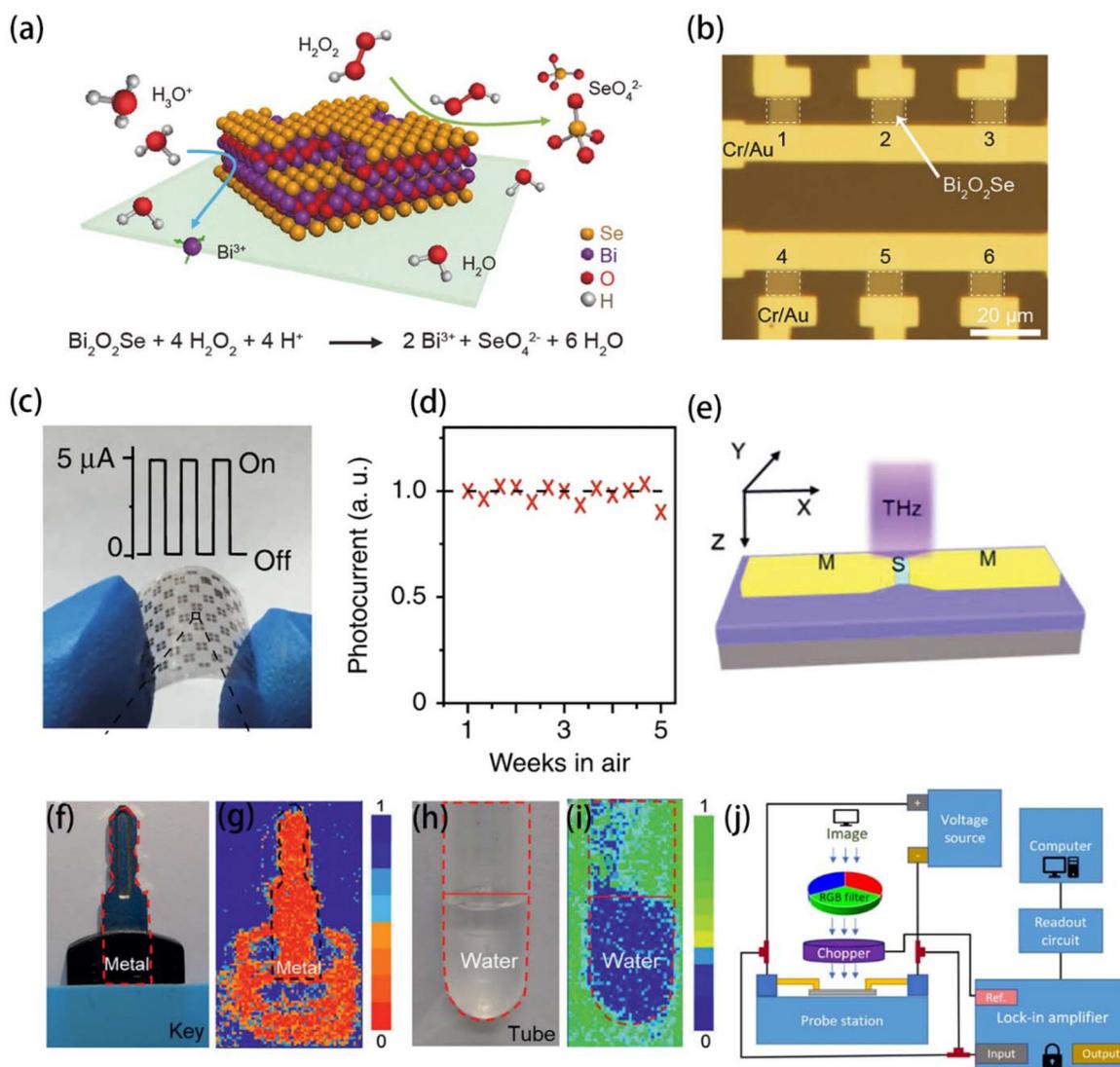
Fig. 8 Photodetection application of 2D Bi$_2$O$_2$Se. (a) Schematic diagram and reaction equation for the etching process of a 2D Bi$_2$O$_2$Se crystal using a mixed solution of H$_2$SO$_4$ and H$_2$O$_2$. (b) Optical image of 2D Bi$_2$O$_2$Se integrated optoelectronic devices prepared on mica substrate, comprising a total of six channels. (c) Photograph of a flexible 2D Bi$_2$O$_2$Se photodetector, with accompanying plots illustrating a typical photoresponse under 1% strain conditions. (d) Consistent stability in photocurrent maintained by the detector over five weeks under ambient conditions. (a–d) Reproduced with permission.[102] Copyright 2020, Wiley. (e) Schematic diagram of the MSM structure of the antenna-assisted terahertz detector. (f) Photograph of a key with a plastic coating. (g) Transmission image of a key in the terahertz range, demonstrating the penetration capability of terahertz light through plastic. (h) Photograph of a test tube containing water. (i) Transmittance photograph of a test tube under THz radiation, demonstrating the strong absorption of THz waves by water. (e–i) Reproduced with permission.[105] Copyright 2021, Wiley. (j) Schematic diagram of a full-color RGB imaging system based on Bi$_2$O$_2$Se nanosheets. Reproduced with permission.[103] Copyright 2023, Springer Nature.

lights the synthesis of high-quality Bi$_2$O$_2$Se as a crucial factor for achieving high performance. On the other hand, Yang et al.,[104] through multi-wavelength light response experiments, confirmed the coexistence of photoconductive and bolometric effects in the Bi$_2$O$_2$Se photodetector. With an increase in incident light power density, the thermal effect gradually strengthened and became dominant. Microscale laser local heating and thermal imaging tracking experiments further verified and were used to study this phenomenon. They hypothesized that this photodetection mechanism was based on temperature-induced thermal carriers or thermoelectrons, rather than

photoexcited electrons and holes. This study provides new insights for the development of radiation thermo-photodetectors.

Table 2 succinctly outlines the photodetection performance of Bi$_2$O$_2$Se and its heterostructures, compared with commercial photodetectors. This comparison provides a precise evaluation of the attributes of Bi$_2$O$_2$Se, demonstrating its broader detection spectrum, higher responsivity, and faster response time, while maintaining equally high air stability—key factors for assessing its performance in photodetection applications.

Table 2 Photodetection performance of 2D Bi_2O_2Se and its heterostructures, including a comparison with commercial materials

Material	Spectral range (nm)	R ($A W^{-1}$)	D^* (Jones)	Response time (ms)	Ref.
Bi_2O_2Se	360–1550	108 696	8.2×10^{12}	32/101	28
Bi_2O_2Se	300–1700	5800	3×10^9	$\sim 10^{-9}$	90
Bi_2O_2Se	532	2.2×10^4	3.4×10^{15}	6	27
Bi_2O_2Se–PbSe	2000	3×10^3	N/A	4	114
Bi_2O_2Se–BP	700–1550	500	2.8×10^{11}	9	115
Bi_2O_2Se–graphene	532	6.5×10^{-3}	N/A	400/310	116
Commercial Si	600–1000	300	10^{13}	N/A	117
Commercial GaAs	400–900	0.53	N/A	N/A	118
Commercial InSe	450–785	12.3	N/A	50	119

5.3. Neuromorphic computing and optoelectronic synapses

Inspired by the biological nervous system, neuromorphic computing aims to simulate and leverage the structure and functionality of neural networks for intelligent computation. This computational model emulates the interconnection and information transmission between biological neurons to achieve tasks such as pattern recognition, learning, and decision-making.[121–123] Owing to their atomic thickness and reduced screening effect, 2D materials offer easily tunable physical properties through techniques like defect engineering, electrostatic doping, chemical intercalation, and strain engineering. These characteristics make them highly promising for neuromorphic computing in synaptic devices.[106–108] Li *et al.*[120] pioneered the applications of Bi_2O_2Se in memristors, constructing an artificial synapse, as shown in Fig. 9a (Fig. 9b depicts a biological synapse). In this structure, modulation of the Bi_2O_2Se channel resistance is achieved by applying a gate voltage to control the charge carriers within the channel. Subsequently, they conducted measurements on this artificial synapse using pulse sequences at different frequencies. The research findings are depicted in Fig. 9c and d. It is noteworthy that this marks the first true coexistence of short-term plasticity (STP) and
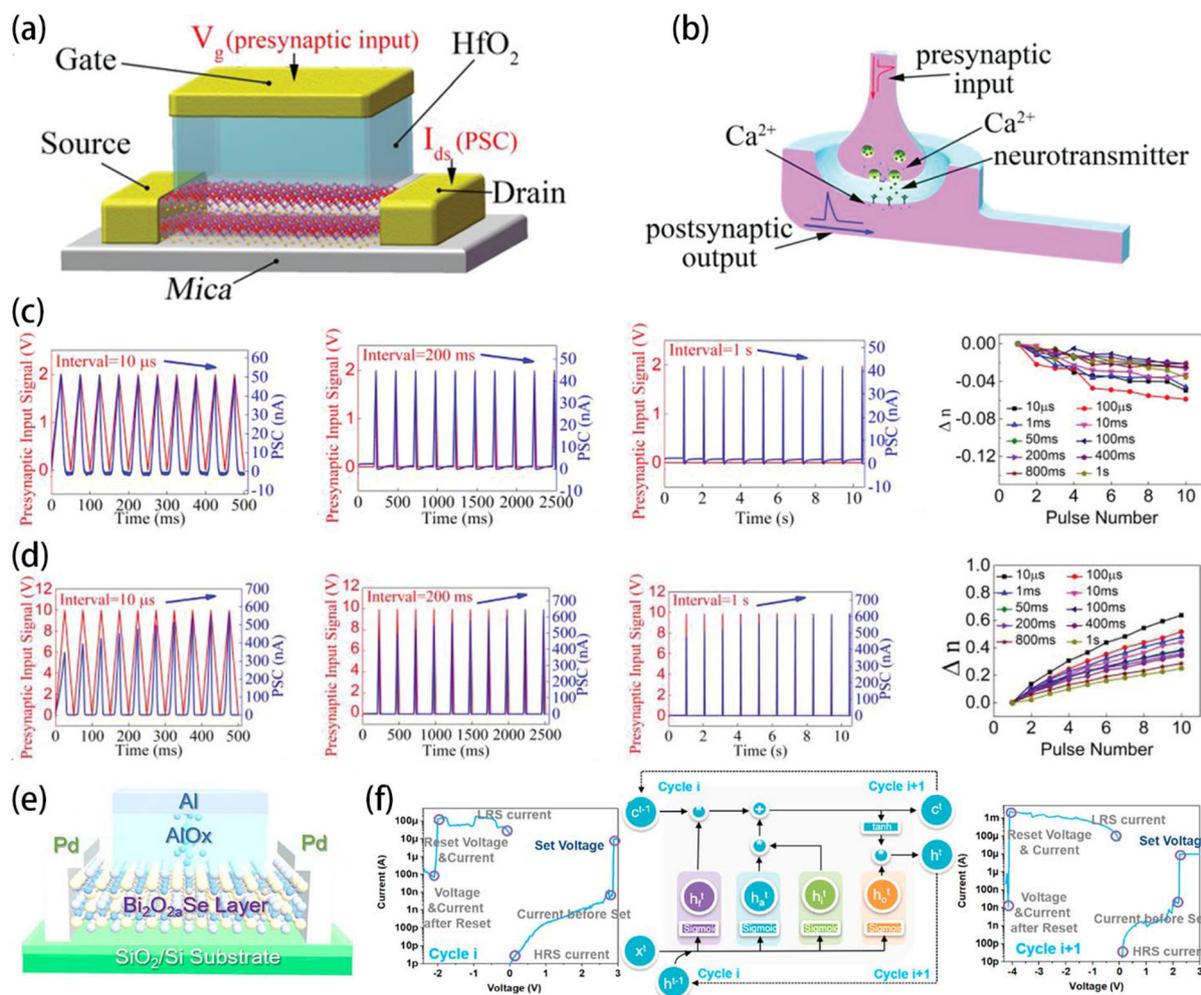
Fig. 9 Application of Bi_2O_2Se in neuromorphic computing. (a) Schematic illustration of the structure of a three-terminal resistive switching device based on Bi_2O_2Se. (b) Schematic of a biological neural synapse. Synaptic devices based on 2D Bi_2O_2Se exhibiting (c) short-term plasticity (STP) and (d) long-term plasticity (LTP). (a–d) Reproduced with permission.[120] Copyright 2018, Wiley. (e) Structure of a Bi_2O_2Se-based resistive random-access memory (RRAM) device used for a TRNG. (f) Switching curve of a Bi_2O_2Se-based memristor in cycle *i* and key parameters for machine learning. (e and f) Reproduced with permission.[110] Copyright 2022, American Chemical Society.

long-term plasticity (LTP) in a three-terminal memristor. Additionally, owing to the complex computing capabilities of this memristor, a "sleep–awake cycle auto-regulation" process can be simulated. In previous memristors based on 2D semiconductors, the coupling of different sites and mechanisms could not be achieved, leading to the controllable induction of STP and LTP or the irreversible transition from STP to LTP.[107,108,124]

Moreover, compared to other two-dimensional material-based memristors, utilizing 2D Bi_2O_2Se as an electrode offers a non-van der Waals interface, high carrier mobility, excellent air stability, extremely low thermal conductivity, and vertical surface resistive switching characteristics, resulting in inherent stochasticity and complexity in memristive true analogue/digital random number generation.[109,110,125,126] Taking advantage of these properties, Liu et al.[110] proposed a true random number generator (TRNG) (Fig. 9e). This device utilizes ampli-

tude-controllable, low-energy random telegraph noise (RTN) signals as an analog true random number generator, applicable for voice encryption and decryption. Furthermore, they applied this device in machine learning research, as shown in Fig. 9f. Simultaneously, the research team verified the efficacy of this random number generator in resisting machine learning predictions, laying the groundwork for providing reliable and unpredictable random keys. Lai et al.[127] utilized CVD-grown Bi_2O_2Se nanosheets as the switching material to construct conductive bridge random access memory (CBRAM) devices, featuring an $Al/Cu/Bi_2O_2Se/Pd$ structure. The operating mechanism is illustrated in Fig. 10a. Under SET conditions, excess Cu ions are generated due to the formation of CuO_x (x = 1, 2) at the Cu/Bi_2O_2Se interface. These Cu ions migrate through layered Bi_2O_2Se and form a conductive filament. Meanwhile, electrons tunnel from the bottom electrode (Pd) through the PdO_x layer, reducing Cu ions at the $Bi_2O_2Se/$
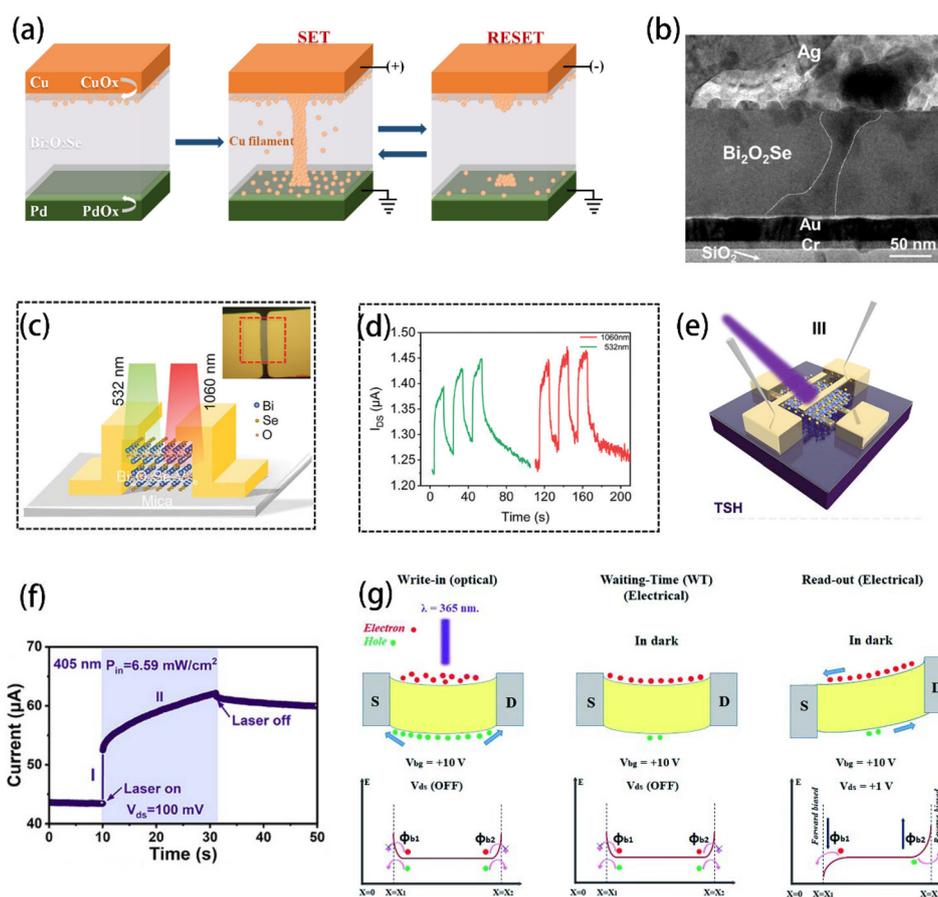

Fig. 10 Application of 2D Bi_2O_2Se in electronic and optoelectronic synapses. (a) Schematic illustration of the switching mechanism and device states under SET and RESET conditions. Reproduced with permission.[127] Copyright 2023, Elsevier. (b) Cross-sectional TEM image of the device. Area of the white line corresponds to Ag conductive filaments. Reproduced with permission.[128] Copyright 2023, American Chemical Society. (c) Schematic diagram of the optical synaptic device based on $Bi_2O_2Se–V_{Se}$. Inset shows an optical image of the device. (d) Typical memory retention behavior after turning off the light under illumination at 532 nm and 1060 nm. (c and d) Reproduced with permission.[70] Copyright 2023, Wiley. (e) Schematic illustration of the three TSH devices obtained, which have a top surface channel. (f) Typical photoresponse of the TSH Bi_2O_2Se devices. (e and f) Reproduced with permission.[130] Copyright 2024, Wiley. (g) Energy band diagram (with a Schottky barrier profile) representing the mechanism of an optoelectronic memory process. This process involves electron trapping at the SiO_2 surface after UV illumination and charge release facilitated by a +1 V read-out bias. Reproduced with permission.[129] Copyright 2022, Royal Society of Chemistry.

PdO$_x$ interface, thus completing the switching process. Similarly, Hu et al.[128] adopted a comparable approach to fabricate Ag/Bi$_2$O$_2$Se/Au two-terminal bipolar memristors, where the formation of Ag conductive filaments was observed under applied voltage (Fig. 10b).

Similar to neuromorphic computing, optoelectronic synapses combined both the electrical and optical properties of materials for information processing and storage. Various strategies have been employed to introduce memory effects into 2D Bi$_2$O$_2$Se-based optoelectronic synapses, including the intentional introduction of defects,[70] device structure design,[129,130] and the incorporation of trapping layers.[129,131,132] Ren et al.[70] used PVD to fabricate Bi$_2$O$_2$Se flakes with a high concentration of V_{Se}, designing an optoelectronic synaptic device (Fig. 10c) that exhibited a persistent photoconductivity (PPC) effect induced by selenium vacancies. By modulating the duration of light exposure, the device can switch between long-term and short-term memory storage. In an array based on this device, after 100 s of illumination at 532 and 1060 nm, the image pattern intensity retained 54.64% and 19.31% of the original memory level, respectively (Fig. 10d), even after a 400 s waiting period. Xie et al.[130] developed a dual-crossbar Bi$_2$O$_2$Se device for various optoelectronic applications, featuring a highly integrated three-in-one configuration: bottom surface horizontal (BSH), middle sandwich vertical (MSV), and top surface horizontal (TSH) devices (Fig. 10e). Their findings indicate that, when illumination ceases, the current in the TSH device does not drop sharply due to the presence of bolometric effects, demonstrating non-volatile characteristics, as shown in Fig. 10f. Lai et al.[129] utilized SiO$_2$ as a trapping layer, where the presence of trapping sites, including dangling bonds on its surface, made it an effective medium for capturing charges and delaying their release. The corresponding energy band diagram during device operation is illustrated in Fig. 10g. This approach of using surface-activated SiO$_2$ as a trapping layer was similarly applied in optoelectronic synapses based on other 2D materials, showing comparable benefits in charge trapping and memory effects.[131,132]

6. Heterostructures and their applications

Despite the excellent electronic properties of Bi$_2$O$_2$Se, practical device applications are challenged by issues such as high carrier concentration and the radiation thermal effect,[24] which lead to increased dark current, decreased photoresponsivity, and slowed response speed. These factors are considered unfavorable in the low-power photonics field. In addition, the intrinsic band gap of Bi$_2$O$_2$Se limits its applications in the broad infrared spectrum. To address these challenges, constructing heterostructures of 2D materials has been proposed as a solution. By forming heterostructures with other materials, including quantum dots,[114] nanowires,[133,134] and other 2D materials such as graphene[116] or TMDs,[135] the carrier concentration, carrier type, and band structure of the heterostructure can be effectively tuned, leading to a significant enhancement in its performance. A heterojunction refers to the interface formed between different crystal structures in semiconductor materials. Their design and construction can change the electrical and optical properties of the materials, providing a wide range of possibilities for the development of new devices. In this section, we focus on the research progress made in 2D Bi$_2$O$_2$Se heterostructures, encompassing various heterostructure types (such as 0D–2D, 1D–2D, 2D–2D), construction methods, and potential applications in specific fields.

6.1. 0D (quantum dots)–2D heterostructure

Due to the exciton coupling that can occur at the interface between quantum dots and 2D materials,[136] leading to enhanced optical responses, 0D–2D heterojunctions typically exhibit superior performance in optoelectronic devices. Narrow-band-gap semiconductor colloidal quantum dots (CQDs) like PbS, PbSe, HgTe, and HgSe are widely used in photodetectors due to their high extinction coefficients and tunable band gaps. When integrated with 2D materials, these composite structures offer the additional advantage of broadening the response spectrum, making them highly effective for advanced photodetection applications.[137–139] In previous studies, some researchers successfully achieved a detection rate of up to 10^7 A W^{-1} by utilizing the heterojunction interface formed by PbS quantum dots and graphene.[137] These previous works provide valuable insights into the construction of Bi$_2$O$_2$Se heterostructures. However, achieving a well-aligned energy band interface between Bi$_2$O$_2$Se and narrow-band-gap quantum dots remains a challenging task. Luo et al.[114] successfully constructed a 0D–2D heterostructure by combining PbSe quantum dots with 2D Bi$_2$O$_2$Se, achieving the efficient detection of infrared light with wavelengths beyond 2 μm. Initially, they synthesized 2D Bi$_2$O$_2$Se on a mica substrate via CVD, followed by direct assembly of PbSe quantum dots using spin-coating. After each cycle, sulfur-diethylamine (EDT) solution was added for ligand exchange, and the samples underwent brief heat treatment at 95 °C to improve neck connections and carrier mobility in the PbSe quantum dots. The process is illustrated in Fig. 11a. Fig. 11b and c present AFM and HR-TEM images of the heterojunction interface. To elucidate the band structure at the interface, researchers conducted ultraviolet photoelectron spectroscopy (UPS) measurements to obtain the work functions of each component. Based on these experimental data, they proposed the band structure model as depicted in Fig. 11d. Below 1000 nm, the device exhibited enhanced light absorption capabilities due to the introduction of PbSe CQDs, demonstrating a 2–5 times improvement in responsivity. Compared to bare Bi$_2$O$_2$Se-based photodetectors, the presence of PbSe quantum dots enables the hybrid detector to maintain high responsivity at wavelengths exceeding 1500 nm (Fig. 11e). However, due to synthesis challenges and the presence of unfavorable interface states, research on quantum dot-modified 2D Bi$_2$O$_2$Se remains limited, and its application potential is yet to be fully explored.
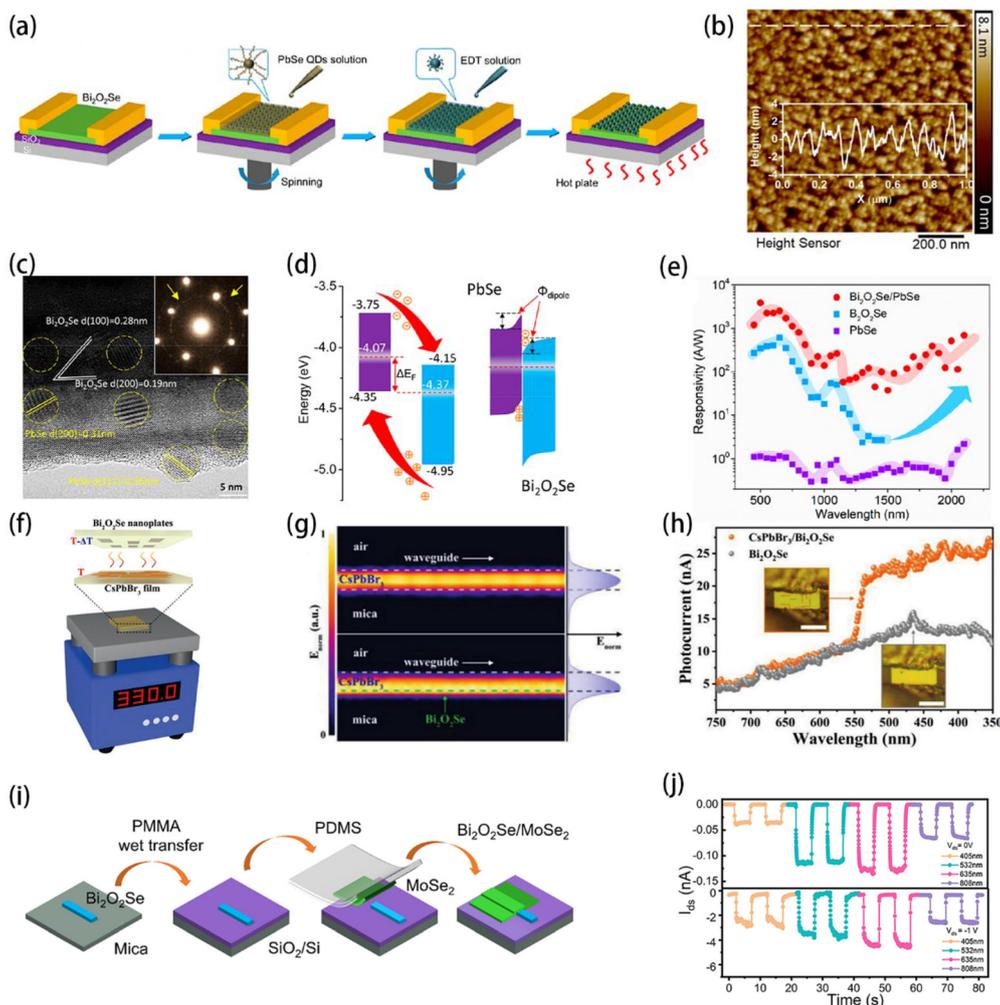
Fig. 11 Mixed-dimensional heterostructures and measurements of photodetection. (a) Schematic diagram of PbSe quantum dot-sensitized Bi_2O_2Se fabricated by a spin-coating process. (b) Surface PbSe quantum dots on Bi_2O_2Se nanosheets captured with high-resolution AFM. (c) HR-TEM image of the heterostructure; inset shows a magnified view, with an arrow pointing to diffraction rings in the SAED pattern, indicating their correlation with randomly oriented PbSe CQDs. (d) Schematic representation of the band structure of the PbSe/Bi_2O_2Se heterojunction. It is anticipated that a charge transfer dipole may form at the PbSe/Bi_2O_2Se interface, potentially impeding electron transfer under photoexcitation to a certain extent. (e) Wavelength-dependent responsivity functions of three material types; PbSe/Bi_2O_2Se hybrid photodetector demonstrates superior responsivity. (a−e) Reproduced with permission.[114] Copyright 2019, American Chemical Society. (f) Schematic diagram of the process for obtaining vertically aligned $CsPbBr_3$ nanowires *via* PVD. (g) Simulated electric field distribution for both pure $CsPbBr_3$ wires (top) and $CsPbBr_3$/Bi_2O_2Se heterostructure waveguides (bottom). (h) Photocurrent of the device as a function of wavelength measured before and after the removal of $CsPbBr_3$. (f−h) Reproduced with permission.[133] Copyright 2021, Wiley. (i) Schematic of the transfer and construction process of the Bi_2O_2Se/$MoSe_2$ heterostructure. (j) Time-resolved photoresponse characteristics of the heterojunction device investigated across different wavelengths, maintaining a constant light power density (405 nm: 22.47 mW cm^{-2}, 532 nm: 17.32 mW cm^{-2}, 635 nm: 20.43 mW cm^{-2}, 808 nm: 26.43 mW cm^{-2}) at both V_{ds} = 0 and −1 V. (i and j) Reproduced with permission.[134] Copyright 2023, American Chemical Society.

6.2. 1D (nanowires)–2D heterostructure

The 1D–2D heterostructure has attracted widespread attention in electronic devices due to the synergistic advantages of the high electron mobility of one-dimensional structures and the large surface area of two-dimensional structures.[140–142] Simultaneously, the direct epitaxial growth of semiconductor nanowires on 2D materials has shown the prospect of achieving the large-scale and facile preparation of 1D/2D heterostructures, as it eliminates the need for sophisticated auxiliary instruments.[143] Fan *et al.*[133] achieved the direct epitaxial

growth of $CsPbBr_3$ nanowires on Bi_2O_2Se nanosheets using a two-step vapor deposition method. Firstly, they pre-grew Bi_2O_2Se nanosheets through CVD. Subsequently, employing a vertical physical vapor deposition (PVD) method, they fabricated a one-dimensional $CsPbBr_3$ nanowire/two-dimensional Bi_2O_2Se nanosheet mixed-dimensional heterostructure, as illustrated in Fig. 11f.

Subsequently, they measured the optical properties of the $CsPbBr_3$/Bi_2O_2Se mixed-dimensional heterostructure through PL spectra. The research results indicate that $CsPbBr_3$ nanowires can act as optical waveguides, guiding light propagation

to both ends (Fig. 11g). To further validate the impact of the optical waveguide on Bi_2O_2Se, they measured the device's photoresponse before and after removing $CsPbBr_3$ nanowires using deionized (DI) water. The results (Fig. 11h) demonstrate that the photocurrent of the device is nearly doubled in the wavelength range of 350 to 540 nm. The wavelength of enhanced photocurrent corresponds to the absorption edge of $CsPbBr_3$ (approximately 550 nm).[144] At a power density of 2 μW cm^{-2}, the device achieved a responsivity of 145 A W^{-1} and a detectivity of 1.02×10^{12} Jones. Chen et al.[134] successfully synthesized Bi_2O_2Se nanowires on mica, transferred them onto Si/SiO_2 substrates, and constructed a mixed-dimensional vdW heterojunction with exfoliated $MoSe_2$ to fabricate a FET device (Fig. 11i), achieving a dark current as low as 4.02×10^{-14} A at −1 V bias and a switching ratio of 3.2×10^3 with a response time of 30 ms (Fig. 11j). These studies provide both theoretical and practical foundations for the application of 1D/2D heterostructures in optoelectronic systems.

6.3. 2D–2D heterostructure

With the continuous prediction and discovery of two-dimensional materials, along with a deeper understanding and optimization of the band characteristics of 2D heterostructures, experimental phenomena have been better explained. In this realm, the outstanding momentum matching and band alignment between two-dimensional black phosphorus (BP) and Bi_2O_2Se serve as the foundation for the exceptional performance of Bi_2O_2Se/BP heterostructured devices.[147] Liu et al.[115] engineered a high-performance broadband photodetector by successfully creating a Bi_2O_2Se/BP van der Waals heterostructure. The research team transferred CVD-grown Bi_2O_2Se onto a Si/SiO_2 substrate, followed by the transfer of exfoliated BP, achieving construction of the heterostructure. While similar to methods used for constructing mixed-dimensional heterostructures, this process successfully overlaid the two-dimensional layers, forming the Bi_2O_2Se/BP heterostructure. Following photoelectric performance assessments, the researchers generated band diagrams under diverse biases (Fig. 12a). Owing to the attributes of low dark current and effective charge carrier separation within the heterostructure, the Bi_2O_2Se/BP device demonstrated remarkable responsivities (R) at wavelengths of 700 nm, 1310 nm, and 1550 nm, achieving approximately ~500 A W^{-1}, ~4.3 A W^{-1}, and ~2.3 A W^{-1}, respectively. Additionally, the specific detectivities (D^*) attained values of ~2.8×10^{11} Jones (700 nm), ~2.4×10^9 Jones (1310 nm), and ~1.3×10^9 Jones (1550 nm), as illustrated in Fig. 12b. It is noteworthy that the response time is approximately ~9 ms, surpassing that of standalone BP (~190 ms) and Bi_2O_2Se (~180 ms) devices by over 20 times. This result distinctly underscores the successful enhancement of the performance of the photodetector through the construction of the Bi_2O_2Se/BP heterostructure.

Chen et al.[116] successfully prepared Bi_2O_2Se/graphene composite materials using a composite molten salt method (CMS) and the reduction of graphene oxide. They constructed a flexible photodetector based on this composite, employing a

solid-state electrolyte as a crucial component of the photodetector, resulting in significant advancements in both flexibility and self-powered capabilities, as illustrated in Fig. 12c. Researchers attributed the changes in the shape of the photocurrent image to minor cracks induced by bending and the less tight contact between the solid electrolyte and the material after multiple folding events. Lyu et al.[148] proposed a design utilizing Bi_2O_2Se/Xene heterostructures, where Xene includes graphene and silicene, and simulated their application in steep-slope transistors. By fully leveraging the linearly decreasing density of states (DOS) of p-type doped Dirac semi-metals and excellent electrostatic gate control at the Bi_2O_2Se/Xene interface, they successfully achieved super-exponential decay of carrier injection, effectively eliminating the thermal tail issue of the Boltzmann distribution, and significantly reducing device power consumption.

Benefiting from the exceptionally strong light–matter interactions of 2D TMDs,[149] the heterojunction formed between Bi_2O_2Se and 2D TMDs presents significant potential for the enhancement of the optoelectronic properties. Lu et al.[145] theoretically presented the ferroelectricity and strain tuning of $MoSe_2$/Bi_2O_2Se van der Waals heterostructures through DFT calculations. They constructed a broken symmetrical model of monolayer Bi_2O_2Se by altering the position of surface Se atoms to induce ferroelectricity. The study also involved strain tuning in $MoSe_2$/Bi_2O_2Se heterostructures, showing that stress could alter the band gap and carrier concentration of the heterostructure, inducing a transition between II-type and I-type band alignments, as shown in Fig. 12d. This tunability provides important prospects for the application of multifunctional ferroelectric photodetectors. Lai et al.[135] introduced a high-speed, broadband fiber-integrated avalanche photodetector based on WS_2/Bi_2O_2Se thin films. The researchers peeled off films from bulk Bi_2O_2Se and WS_2 using Scotch tape and then precisely transferred the WS_2 and Bi_2O_2Se target films onto the end facet of an optical fiber through microscale manipulation, forming the WS_2/Bi_2O_2Se heterostructure. The device exhibited a remarkable photoresponsivity of up to 1.13 A W^{-1} and a rapid response speed of 410/600 μs. The sensitivity of the optical fiber-integrated device to light intensity suggests extensive applications in bend deformation measurements. Fig. 12e illustrates the variation in photocurrent, effectively reflecting the degree of wrist bending. When the pigtailed optical fiber is bent, total internal reflection conditions are disrupted, causing light to escape from the optical fiber and resulting in a reduction in photocurrent. In a subsequent study by Chitara et al.,[150] they delved into the heterostructure formed by V-doped WS_2 and Bi_2O_2Se. Results from PL spectra indicated that V-doped WS_2/Bi_2O_2Se exhibited a higher charge transfer efficiency, and the exciton binding energy in the V–WS_2/Bi_2O_2Se heterostructure was significantly lower than that in monolayer WS_2. These findings suggest superior optoelectronic performance in the device.

A recent study reported the development of a UV-assisted in situ oxidation process to obtain vertically aligned Bi_2O_2Se–Bi_2SeO_5 heterojunctions with atomically flat interfaces, where
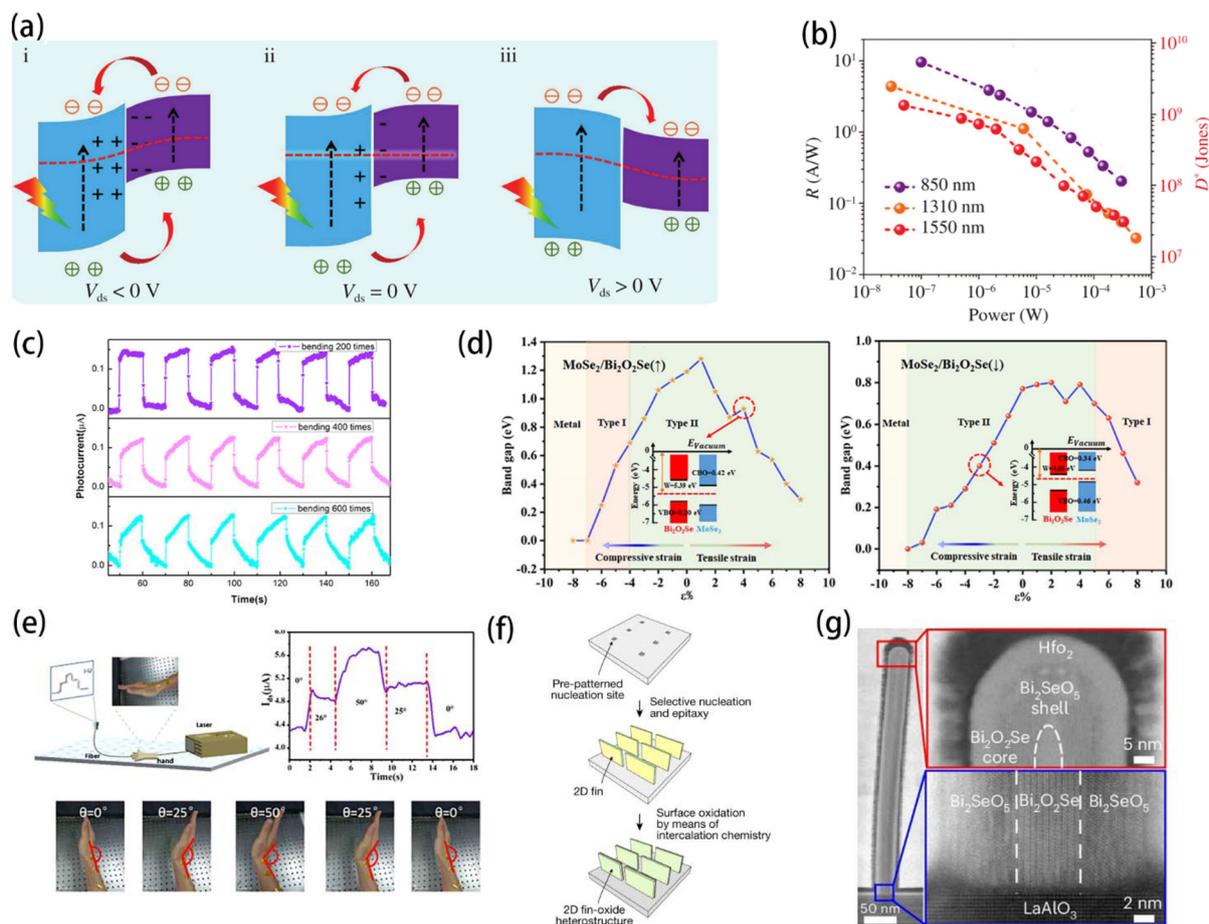
Fig. 12 Bi_2O_2Se 2D–2D heterostructures. (a) Band diagrams of the BP/Bi_2O_2Se heterostructure under positive bias (i), zero bias (ii), and negative bias (iii) conditions. (b) Responsivity and detectivity of the Bi_2O_2Se/BP vdW heterojunction photodetector as a function of incident light power at wavelengths of 850 nm, 1310 nm, and 1550 nm under a bias voltage of −1 V. (a and b) Reproduced with permission.[115] Copyright 2021, Springer Nature. (c) Graphs of the photocurrent in the device after various bending cycles demonstrate excellent stability. Reproduced with permission.[116] Copyright 2021, Elsevier. (d) Band gaps of $MoSe_2$/Bi_2O_2Se under in-plane biaxial strain. Insets show the band alignments of $MoSe_2$/Bi_2O_2Se heterostructures with different stacking modes. Reproduced with permission.[145] Copyright 2023, Royal Society of Chemistry. (e) Figures of the WS_2/Bi_2O_2Se fiber-integrated photodetector for bending measurements, depicting varying photocurrents at different bending angles. Reproduced with permission.[135] Copyright 2023, Elsevier. (f) Schematic diagram of the synthesis process for the vertical Bi_2O_2Se–Bi_2SeO_5 fin heterojunction. Reproduced with permission.[23] Copyright 2023, Springer Nature. (g) Cross-sectional STEM images of a 2D Bi_2O_2Se–Bi_2SeO_5 fin-oxide heterostructure coated with a HfO_2 dielectric layer. Reproduced with permission.[146] Copyright 2024, Springer Nature.

Bi_2SeO_5 acted as a high-k gate oxide,[151] facilitating the construction of high-performance fin FETs.[23,146,152] The researchers first grew vertical 2D Bi_2O_2Se by depositing seed layers and selecting abnormal insulating oxide substrates with low symmetry, such as $LaAlO_3$ (110) and MgO (110), where vertical 2D Bi_2O_2Se exhibited a significantly lower binding energy than the planar form. Subsequently, a UV-assisted intercalation oxidation method was employed to directly synthesize the 2D Bi_2O_2Se–Bi_2SeO_5 fin-oxide heterostructure *in situ* (Fig. 12f and g). This heterojunction with atomically flat interfaces significantly enhances the device performance, offering new possibilities and directions for the further extension of Moore's law.

However, most Bi_2O_2Se-based 2D–2D heterojunctions are currently obtained through exfoliation methods, which often result in unexpected interface defects. Therefore, *in situ* syn-

thesis methods for heterojunctions are highly desirable. For instance, by adjusting precursors during the CVD process, 2D Bi_2O_2Se–Bi_2O_2X heterojunctions can be grown, and the growth mode—whether vertical or planar—can be controlled by varying the growth conditions.[153,154]

7. Summary and prospects

In conclusion, we have provided a comprehensive overview of Bi_2O_2Se, covering its physical characteristics, structural properties, synthesis methods, and applications, while highlighting the latest advancements in research. We began by presenting its structure, encompassing the crystal structure, electronic band structure, and physical characteristics. Subsequently, we

summarized a series of approaches to modulate its physical properties, such as thickness tuning, defect engineering, and the variations in the properties of Bi_2O_2Se under stress. Due to the diverse synthesis challenges and structural requirements of Bi_2O_2Se, various methods have been reported for producing 2D Bi_2O_2Se, including mechanical exfoliation, MBE, CVD, and PLD. Additionally, we highlighted the potential applications of Bi_2O_2Se in FETs, photodetectors, neuromorphic computing and optoelectronic synapses. Finally, we explored the construction of heterojunctions involving Bi_2O_2Se with other materials, including 0D–2D, 1D–2D, and 2D–2D heterojunctions, leveraging the excellent tunability of electronic properties and surface effects in 2D materials to significantly enhance the performance of hybrid devices.

Despite considerable advancements in Bi_2O_2Se research, it remains in the initial phases with various challenges yet to be addressed. Foremost among these challenges is the quest for a cost-effective and scalable method for producing high-quality Bi_2O_2Se. Unlike most 2D materials, the interlayer force of Bi_2O_2Se is electrostatic, making it challenging to obtain layered Bi_2O_2Se through a simple mechanical exfoliation method. Although the widely used CVD method can synthesize high-quality 2D Bi_2O_2Se, its slow synthesis speed and low yield make it less applicable for industrial production. Therefore, future efforts should focus on developing synthesis methods that can accurately control the desired material properties while maintaining high productivity. Secondly, further in-depth research is needed on the precise control of the physical properties of Bi_2O_2Se. Current studies primarily focus on controlling the thickness and defects, with relatively few experimental reports specifically investigating how these factors affect the electrical and optical properties of Bi_2O_2Se and intentionally tuned defects. Thirdly, more research is eagerly awaited on Bi_2O_2Se heterostructures and their devices. Various techniques for preparing Bi_2O_2Se heterostructures have not been standardized yet and standardizing the preparation process will contribute to improving the repeatability and controllability of devices. Simultaneously, integrating Bi_2O_2Se heterostructure devices into practical applications may require addressing integration and packaging issues to ensure stability in various environments. Lastly, the applications of Bi_2O_2Se need further expansion and deepening. Currently, most research on Bi_2O_2Se is concentrated in the field of optoelectronic detection, while studies in other areas such as FETs and lasers have not reached a mature stage. The maturity of these devices still lags behind industrial and commercial standards. Future research directions may include more applications integrated with traditional materials like silicon. Despite these challenges, the promising performance of Bi_2O_2Se suggests a vast development prospect.

Author contributions

Xiaoyu Hu: conceptualization, writing – original draft, writing – review and editing; Wen He: supervision, review and editing; Dongbo Wang: supervision; Lei Chen, Xiangqian Fan and Duoduo Ling: formal analysis, conceptualization; Yanghao Bi and Wei Wu: writing – review & editing, resources; Shuai Ren and Ping Rong: review and editing; Yinze Zhang and Yajie Han: writing – original draft; Jinzhong Wang: funding acquisition, supervision, review and editing, project administration.

Data availability

Data availability is not applicable to this article as no new data were created or analyzed in this study. The data in this article are derived from references.

Conflicts of interest

There are no conflicts of interest to declare.

Acknowledgements

References

1 M. Long, P. Wang, H. Fang and W. Hu, *Adv. Funct. Mater.*, 2019, **29**, 1803807.
2 C. Downs and T. E. Vandervelde, *Sensors*, 2013, **13**, 5054–5098.
3 D. J. Buckley, N. C. Black, E. G. Castanon, C. Melios, M. Hardman and O. Kazakova, *2D Mater.*, 2020, **7**, 032002.
4 X. Chen, M. Leishman, D. Bagnall and N. Nasiri, *Nanomaterials*, 2021, **11**, 1927.
5 N. Isaac, I. Pikaar and G. Biskos, *Microchim. Acta*, 2022, **189**, 196.
6 Y. Khan, A. E. Ostfeld, C. M. Lochner, A. Pierre and A. C. Arias, *Adv. Mater.*, 2016, **28**, 4373–4395.
7 S. Z. Butler, S. M. Hollen, L. Cao, Y. Cui, J. A. Gupta, H. R. Gutiérrez, T. F. Heinz, S. S. Hong, J. Huang and A. F. Ismach, *ACS Nano*, 2013, **7**, 2898–2926.
8 T. Vincent, J. Liang, S. Singh, E. G. Castanon, X. Zhang, A. McCreary, D. Jariwala, O. Kazakova and Z. Y. Al Balushi, *Appl. Phys. Rev.*, 2021, **8**, 041320.
9 Y. Qi, M. A. Sadi, D. Hu, M. Zheng, Z. Wu, Y. Jiang and Y. P. Chen, *Adv. Mater.*, 2023, **35**, 2205714.
10 Q. Ma, G. Ren, K. Xu and J. Z. Ou, *Adv. Opt. Mater.*, 2021, **9**, 2001313.
11 C. Tan, X. Cao, X.-J. Wu, Q. He, J. Yang, X. Zhang, J. Chen, W. Zhao, S. Han and G.-H. Nam, *Chem. Rev.*, 2017, **117**, 6225–6331.
12 F. Schwierz, *Nat. Nanotechnol.*, 2010, **5**, 487–496.

13 S. Zhang, J. Yang, R. Xu, F. Wang, W. Li, M. Ghufran, Y.-W. Zhang, Z. Yu, G. Zhang and Q. Qin, *ACS Nano*, 2014, **8**, 9590–9596.

14 J. O. Island, G. A. Steele, H. S. van der Zant and A. Castellanos-Gomez, *2D Mater.*, 2015, **2**, 011002.

15 Z. Ni, M. Ye, J. Ma, Y. Wang, R. Quhe, J. Zheng, L. Dai, D. Yu, J. Shi and J. Yang, *Adv. Electron. Mater.*, 2016, **2**, 1600191.

16 X. Yang, L. Qu, F. Gao, Y. Hu, H. Yu, Y. Wang, M. Cui, Y. Zhang, Z. Fu and Y. Huang, *ACS Appl. Mater. Interfaces*, 2022, **14**, 7175–7183.

17 P. Rong, S. Gao, M. Zhang, S. Ren, H. Lu, J. Jia, S. Jiao, Y. Zhang and J. Wang, *J. Alloys Compd.*, 2022, **928**, 167128.

18 K. Wang, H. Qiao, J. Li and X. Qi, *Appl. Surf. Sci.*, 2021, **565**, 150444.

19 Q. Wei, C. Lin, Y. Li, X. Zhang, Q. Zhang, Q. Shen, Y. Cheng and W. Huang, *J. Appl. Phys.*, 2018, **124**, 055701.

20 H. Liu, R. Sun and X. Lu, *Inorg. Chem.*, 2023, **62**, 16752–16758.

21 W. Ai, J. Chen, X. Dong, Z. Gao, Y. He, Z. Liu, H. Fu, F. Luo and J. Wu, *Nano Lett.*, 2022, **22**, 7659–7666.

22 X. Zou, H. Liang, Y. Li, Y. Zou, F. Tian, Y. Sun and C. Wang, *Adv. Funct. Mater.*, 2023, **33**, 2213807.

23 C. Tan, M. Yu, J. Tang, X. Gao, Y. Yin, Y. Zhang, J. Wang, X. Gao, C. Zhang and X. Zhou, *Nature*, 2023, **616**, 66–72.

24 J. Wu, H. Yuan, M. Meng, C. Chen, Y. Sun, Z. Chen, W. Dang, C. Tan, Y. Liu and J. Yin, *Nat. Nanotechnol.*, 2017, **12**, 530–534.

25 Q. Fu, C. Zhu, X. Zhao, X. Wang, A. Chaturvedi, C. Zhu, X. Wang, Q. Zeng, J. Zhou and F. Liu, *Adv. Mater.*, 2019, **31**, 1804945.

26 U. Khan, A. Nairan, K. Khan, S. Li, B. Liu and J. Gao, *Small*, 2023, **19**, 2206648.

27 U. Khan, Y. Luo, L. Tang, C. Teng, J. Liu, B. Liu and H. M. Cheng, *Adv. Funct. Mater.*, 2019, **29**, 1807979.

28 T. Tong, Y. Chen, S. Qin, W. Li, J. Zhang, C. Zhu, C. Zhang, X. Yuan, X. Chen and Z. Nie, *Adv. Funct. Mater.*, 2019, **29**, 1905806.

29 Y. Liang, Y. Chen, Y. Sun, S. Xu, J. Wu, C. Tan, X. Xu, H. Yuan, L. Yang and Y. Chen, *Adv. Mater.*, 2019, **31**, 1901964.

30 C. Chen, M. Wang, J. Wu, H. Fu, H. Yang, Z. Tian, T. Tu, H. Peng, Y. Sun and X. Xu, *Sci. Adv.*, 2018, **4**, eaat8355.

31 J. Li, Z. Wang, Y. Wen, J. Chu, L. Yin, R. Cheng, L. Lei, P. He, C. Jiang and L. Feng, *Adv. Funct. Mater.*, 2018, **28**, 1706437.

32 M. Meng, S. Huang, C. Tan, J. Wu, Y. Jing, H. Peng and H. Xu, *Nanoscale*, 2018, **10**, 2704–2710.

33 K. S. Novoselov, A. Mishchenko, A. Carvalho and A. H. Castro Neto, *Science*, 2016, **353**, aac9439.

34 X. Liu and M. C. Hersam, *Adv. Mater.*, 2018, **30**, 1801586.

35 C. Zhao, D. Wang, J. Cao, Z. Zeng, B. Zhang, J. Pan, D. Liu, S. Liu, S. Jiao and T. Chen, *Nano Res.*, 2024, **17**, 1864–1874.

36 C. M. Yang, T. C. Chen, D. Verma, L. J. Li, B. Liu, W. H. Chang and C. S. Lai, *Adv. Funct. Mater.*, 2020, **30**, 2001598.

37 C. Chang, W. Chen, Y. Chen, Y. Chen, Y. Chen, F. Ding, C. Fan, H. J. Fan, Z. Fan and C. Gong, *Wuli Huaxue Xuebao/Acta Phys.-Chim. Sin.*, 2021, 2108017.

38 Q. Wei, R. Li, C. Lin, A. Han, A. Nie, Y. Li, L.-J. Li, Y. Cheng and W. Huang, *ACS Nano*, 2019, **13**, 13439–13444.

39 M. A. Green, *J. Appl. Phys.*, 1990, **67**, 2944–2954.

40 S.-L. Li, K. Tsukagoshi, E. Orgiu and P. Samorì, *Chem. Soc. Rev.*, 2016, **45**, 118–151.

41 W. Zhang, Z. Huang, W. Zhang and Y. Li, *Nano Res.*, 2014, **7**, 1731–1737.

42 J. Qiao, X. Kong, Z.-X. Hu, F. Yang and W. Ji, *Nat. Commun.*, 2014, **5**, 4475.

43 K. Zhao, H. Liu, C. Tan, J. Xiao, J. Shen, G. Liu, H. Peng, L. Lu and F. Qu, *Appl. Phys. Lett.*, 2022, **121**, 212104.

44 S. Liu, C. Tan, D. He, Y. Wang, H. Peng and H. Zhao, *Adv. Opt. Mater.*, 2020, **8**, 1901567.

45 J. Wang, J. Huang, D. Kaplan, X. Zhou, C. Tan, J. Zhang, G. Jin, X. Cong, Y. Zhu and X. Gao, *Nat. Nanotechnol.*, 2024, 1–8.

46 B. W. Baugher, H. O. Churchill, Y. Yang and P. Jarillo-Herrero, *Nano Lett.*, 2013, **13**, 4212–4216.

47 B. Radisavljevic and A. Kis, *Nat. Mater.*, 2013, **12**, 815–820.

48 R. Pisoni, A. Kormányos, M. Brooks, Z. Lei, P. Back, M. Eich, H. Overweg, Y. Lee, P. Rickhaus and K. Watanabe, *Phys. Rev. Lett.*, 2018, **121**, 247701.

49 N. Thillosen, S. Cabanas, N. Kaluza, V. Guzenko, H. Hardtdegen and T. Schäpers, *Phys. Rev. B: Condens. Matter Mater. Phys.*, 2006, **73**, 241311.

50 I. Van Weperen, B. Tarasinski, D. Eeltink, V. Pribiag, S. Plissard, E. Bakkers, L. Kouwenhoven and M. Wimmer, *Phys. Rev. B: Condens. Matter Mater. Phys.*, 2015, **91**, 201413.

51 L. Samuelson, C. Thelander, M. Björk, M. Borgström, K. Deppert, K. Dick, A. Hansen, T. Mårtensson, A. Panev and A. Persson, *Phys. E*, 2004, **25**, 313–318.

52 R. Quhe, J. Liu, J. Wu, J. Yang, Y. Wang, Q. Li, T. Li, Y. Guo, J. Yang and H. Peng, *Nanoscale*, 2019, **11**, 532–540.

53 S. Fan, Y. Wu, W. Li, J. Gao, W. Yang, J. Deng, R. Cao and X. Liu, *Appl. Phys. Lett.*, 2023, **122**, 223503.

54 H. Li, X. Xu, Y. Zhang, R. Gillen, L. Shi and J. Robertson, *Sci. Rep.*, 2018, **8**, 10920.

55 A. L. Pereira, D. Santamaría-Pérez, J. Ruiz-Fuertes, F.-J. Manjón, V. P. Cuenca-Gotor, R. Vilaplana, O. Gomis, C. Popescu, A. Muñoz and P. Rodríguez-Hernández, *J. Phys. Chem. C*, 2018, **122**, 8853–8867.

56 W. Chen, U. Khan, S. Feng, B. Ding, X. Xu and B. Liu, *Adv. Funct. Mater.*, 2020, **30**, 2004960.

57 C.-Y. Hong, G.-F. Huang, W.-W. Yao, J.-J. Deng and X.-L. Liu, *Chin. Phys. B*, 2019, **28**, 128502.

58 Y. Liu, H. Nan, X. Wu, W. Pan, W. Wang, J. Bai, W. Zhao, L. Sun, X. Wang and Z. Ni, *ACS Nano*, 2013, **7**, 4202–4209.

59 M. Gao, W. Wei, T. Han, B. Li, Z. Zeng, L. Luo and C. Zhu, *ACS Appl. Mater. Interfaces*, 2022, **14**, 15370–15380.

60 H. Takahashi, A. Sugimoto, Y. Nambu, T. Yamauchi, Y. Hirata, T. Kawakami, M. Avdeev, K. Matsubayashi, F. Du and C. Kawashima, *Nat. Mater.*, 2015, **14**, 1008–1012.

61 K. Kirshenbaum, P. Syers, A. Hope, N. Butch, J. Jeffries, S. Weir, J. Hamlin, M. Maple, Y. Vohra and J. Paglione, *Phys. Rev. Lett.*, 2013, **111**, 087001.

62 J. Zhang, S. Zhang, H. Weng, W. Zhang, L. Yang, Q. Liu, S. Feng, X. Wang, R. Yu and L. Cao, *Proc. Natl. Acad. Sci. U. S. A.*, 2011, **108**, 24–28.

63 P. Ruleova, C. Drasar, P. Lostak, C.-P. Li, S. Ballikaya and C. Uher, *Mater. Chem. Phys.*, 2010, **119**, 299–302.

64 H. Tian, T. Tu, X. Jin, C. Li, T. Lin, Q. Dong, X. Jing, B. Liu, R. Liu and D. Li, *J. Am. Chem. Soc.*, 2024, **146**(11), 7324–7331.

65 X. Huang, C.-Y. Niu, J. Zhang, A. Wang, Y. Jia and Y. Song, *APL Mater.*, 2019, **7**, 081110.

66 C.-W. Hu, Y. Yang, C. Hou and T.-X. Liang, *Comput. Mater. Sci.*, 2021, **194**, 110424.

67 U. J. Kim, S. H. Nam, J. Seo, M. Yang, Q. Fu, Z. Liu, H. Son, M. Lee and M. G. Hahm, *ACS Nano*, 2022, **16**, 3637–3646.

68 J. Liu, F. Yang, J. Lu, S. Ye, H. Guo, H. Nie, J. Zhang, J. He, B. Zhang and Z. Ni, *Nat. Commun.*, 2022, **13**, 3855.

69 U. Keller, K. J. Weingarten, F. X. Kartner, D. Kopf, B. Braun, I. D. Jung, R. Fluck, C. Honninger, N. Matuschek and J. Aus der Au, *IEEE J. Sel. Top. Quantum Electron.*, 1996, **2**, 435–453.

70 X. Ren, X. He, X. Li, Y. Li, F. Gao, J. Zhang and P. Hu, *Adv. Opt. Mater.*, 2024, **12**, 2302852.

71 F. Yang, H. K. Ng, J. Wu, Y. Zhao and J. Lu, *Sci. China Inform. Sci.*, 2023, **66**, 160408.

72 R. Beams, L. G. Cançado and L. Novotny, *J. Phys.: Condens. Matter*, 2015, **27**, 083002.

73 C. Thomsen and S. Reich, *Phys. Rev. Lett.*, 2000, **85**, 5214.

74 L. Pan, L. Zhao, X. Zhang, C. Chen, P. Yao, C. Jiang, X. Shen, Y. Lyu, C. Lu and L.-D. Zhao, *ACS Appl. Mater. Interfaces*, 2019, **11**, 21603–21609.

75 L. Pan, J. Zhang, C. Chen and Y. Wang, *Scr. Mater.*, 2020, **178**, 376–381.

76 L. Pan, W.-D. Liu, J.-Y. Zhang, X.-L. Shi, H. Gao, Q.-f. Liu, X. Shen, C. Lu, Y.-F. Wang and Z.-G. Chen, *Nano Energy*, 2020, **69**, 104394.

77 S. Ren, S. Gao, P. Rong, L. Li, M. Zhang, H. Lu, J. Yan, D. Ling, S. Jiao and J. Wang, *Chem. Eng. J.*, 2023, **468**, 143626.

78 Y. Song, Z. Li, H. Li, S. Tang, G. Mu, L. Xu, W. Peng, D. Shen, Y. Chen and X. Xie, *Nanotechnology*, 2020, **31**, 165704.

79 L. Qiao, J. H. Jang, D. J. Singh, Z. Gai, H. Xiao, A. Mehta, R. K. Vasudevan, A. Tselev, Z. Feng and H. Zhou, *Nano Lett.*, 2015, **15**, 4677–4684.

80 X. Tan, J.-L. Lan, Y.-C. Liu, G.-K. Ren, C.-C. Zeng, Y.-H. Lin and C. Nan, *J. Electroceram.*, 2016, **37**, 66–72.

81 C. Huang and H. Yu, *ACS Appl. Mater. Interfaces*, 2020, **12**, 19643–19654.

82 A. Y. Cho and J. Arthur, *Prog. Solid State Chem.*, 1975, **10**, 157–191.

83 Y.-Y. Li, G. Wang, X.-G. Zhu, M.-H. Liu, C. Ye, X. Chen, Y.-Y. Wang, K. He, L.-L. Wang and X.-C. Ma, *Adv. Mater.*, 2010, **22**, 4002–4007.

84 R. Munoz and C. Gómez-Aleixandre, *Chem. Vap. Deposition*, 2013, **19**, 297–322.

85 J. B. Smith, D. Hagaman and H.-F. Ji, *Nanotechnology*, 2016, **27**, 215602.

86 J. Zhang, F. Wang, V. B. Shenoy, M. Tang and J. Lou, *Mater. Today*, 2020, **40**, 132–139.

87 K. Mazumder and P. M. Shirage, *J. Alloys Compd.*, 2021, **888**, 161492.

88 Y.-H. Lee, X.-Q. Zhang, W. Zhang, M.-T. Chang, C.-T. Lin, K.-D. Chang, Y.-C. Yu, J. T.-W. Wang, C.-S. Chang and L.-J. Li, *arXiv*, preprint, arXiv:1202.5458, 2012, DOI: **10.48550/arXiv.1202.5458**.

89 A. J. Watson, W. Lu, M. H. Guimarães and M. Stöhr, *2D Mater.*, 2021, **8**, 032001.

90 J. Yin, Z. Tan, H. Hong, J. Wu, H. Yuan, Y. Liu, C. Chen, C. Tan, F. Yao and T. Li, *Nat. Commun.*, 2018, **9**, 3311.

91 Z. Wu, G. Liu, Y. Wang, X. Yang, T. Wei, Q. Wang, J. Liang, N. Xu, Z. Li and B. Zhu, *Adv. Funct. Mater.*, 2019, **29**, 1906639.

92 C. Hong, Y. Tao, A. Nie, M. Zhang, N. Wang, R. Li, J. Huang, Y. Huang, X. Ren and Y. Cheng, *ACS Nano*, 2020, **14**, 16803–16812.

93 X. Zou, Y. Sun and C. Wang, *Small Methods*, 2022, **6**, 2200347.

94 R. U. R. Sagar, U. Khan, M. Galluzzi, S. Aslam, A. Nairan, T. Anwar, W. Ahmad, M. Zhang and T. Liang, *ACS Appl. Electron. Mater.*, 2020, **2**, 2123–2131.

95 Y. Jiang, X. Zhang, Y. Wang, N. Wang, D. West, S. Zhang and Z. Zhang, *Nano Lett.*, 2015, **15**, 3147–3152.

96 C. Tan, M. Tang, J. Wu, Y. Liu, T. Li, Y. Liang, B. Deng, Z. Tan, T. Tu and Y. Zhang, *Nano Lett.*, 2019, **19**, 2148–2153.

97 A. Koh, Y. Foong and D. H. Chua, *Appl. Phys. Lett.*, 2010, **97**, 114102.

98 M. I. Serna, S. H. Yoo, S. Moreno, Y. Xi, J. P. Oviedo, H. Choi, H. N. Alshareef, M. J. Kim, M. Minary-Jolandan and M. A. Quevedo-Lopez, *ACS Nano*, 2016, **10**, 6054–6061.

99 J. Yao, Z. Zheng, J. Shao and G. Yang, *Nanoscale*, 2015, **7**, 14974–14981.

100 D. Velázquez, R. Seibert, H. Man, L. Spentzouris and J. Terry, *J. Appl. Phys.*, 2016, **119**, 095306.

101 J. Yang, R. Quhe, Q. Li, S. Liu, L. Xu, Y. Pan, H. Zhang, X. Zhang, J. Li and J. Yan, *Adv. Electron. Mater.*, 2019, **5**, 1800720.

102 J. Wu, Y. Liu, Z. Tan, C. Tan, J. Yin, T. Li, T. Tu and H. Peng, *Adv. Mater.*, 2017, **29**, 1704060.

103 H. Wang, S. Zhang, X. Wu, H. Luo, J. Liu, Z. Mu, R. Liu, G. Yuan, Y. Liang and J. Tan, *Nano Res.*, 2023, **16**, 7638–7645.

104 H. Yang, C. Tan, C. Deng, R. Zhang, X. Zheng, X. Zhang, Y. Hu, X. Guo, G. Wang and T. Jiang, *Small*, 2019, **15**, 1904482.

105 Y. Chen, W. Ma, C. Tan, M. Luo, W. Zhou, N. Yao, H. Wang, L. Zhang, T. Xu and T. Tong, *Adv. Funct. Mater.*, 2021, **31**, 2009554.

106 J. J. Yang, D. B. Strukov and D. R. Stewart, *Nat. Nanotechnol.*, 2013, **8**, 13–24.

107 G. Cao, P. Meng, J. Chen, H. Liu, R. Bian, C. Zhu, F. Liu and Z. Liu, *Adv. Funct. Mater.*, 2021, **31**, 2005443.

108 G. Lee, J. H. Baek, F. Ren, S. J. Pearton, G. H. Lee and J. Kim, *Small*, 2021, **17**, 2100640.

109 A. Oberoi, A. Dodda, H. Liu, M. Terrones and S. Das, *ACS Nano*, 2021, **15**, 19815–19827.

110 B. Liu, Y.-F. Chang, J. Li, X. Liu, L. A. Wang, D. Verma, H. Liang, H. Zhu, Y. Zhao and L.-J. Li, *ACS Nano*, 2022, **16**, 6847–6857.

111 Y. Zhang, J. Yu, R. Zhu, M. Wang, C. Tan, T. Tu, X. Zhou, C. Zhang, M. Yu and X. Gao, *Nat. Electron.*, 2022, **5**, 643–649.

112 S. Liu, L. Xu, Y. Pan, J. Yang, J. Li, X. Zhang, L. Xu, H. Pang, J. Yan and B. Shi, *Adv. Theory Simul.*, 2019, **2**, 1800178.

113 L. Xu, S. Liu, J. Yang, B. Shi, Y. Pan, X. Zhang, H. Li, J. Yan, J. Li and L. Xu, *J. Phys. Chem. C*, 2019, **123**, 8923–8931.

114 P. Luo, F. Zhuge, F. Wang, L. Lian, K. Liu, J. Zhang and T. Zhai, *ACS Nano*, 2019, **13**, 9028–9037.

115 X. Liu, W. Wang, F. Yang, S. Feng, Z. Hu, J. Lu and Z. Ni, *Sci. China Inform. Sci.*, 2021, **64**, 1–7.

116 G. Chen, Y. Zhou, G. Zhang, J. Li and X. Qi, *Ceram. Int.*, 2021, **47**, 25255–25263.

117 J. R. Manders, T. H. Lai, Y. An, W. Xu, J. Lee, D. Y. Kim, G. Bosman and F. So, *Adv. Funct. Mater.*, 2014, **24**, 7205–7210.

118 *High Speed Photodetector, 400–900 nm Battery Biased GaAs Detector, 12.5 GHz*, https://www.newport.com.cn/p/818-BB-45.

119 S. R. Tamalampudi, Y.-Y. Lu, R. K. U, R. Sankar, C.-D. Liao, C.-H. Cheng, F. C. Chou and Y.-T. Chen, *Nano Lett.*, 2014, **14**, 2800–2806.

120 Z. Zhang, T. Li, Y. Wu, Y. Jia, C. Tan, X. Xu, G. Wang, J. Lv, W. Zhang and Y. He, *Adv. Mater.*, 2019, **31**, 1805769.

121 C. Liu, H. Chen, S. Wang, Q. Liu, Y.-G. Jiang, D. W. Zhang, M. Liu and P. Zhou, *Nat. Nanotechnol.*, 2020, **15**, 545–557.

122 V. K. Sangwan and M. C. Hersam, *Nat. Nanotechnol.*, 2020, **15**, 517–528.

123 L. Abbott and W. G. Regehr, *Nature*, 2004, **431**, 796–803.

124 X. Yan, Q. Zhao, A. P. Chen, J. Zhao, Z. Zhou, J. Wang, H. Wang, L. Zhang, X. Li and Z. Xiao, *Small*, 2019, **15**, 1901423.

125 W. Huh, D. Lee and C. H. Lee, *Adv. Mater.*, 2020, **32**, 2002092.

126 Y. Zhao, Z. Lou, J. Hu, Z. Li, L. Xu, Z. Chen, Z. Xu, T. Wang, M. Wu and H. Ying, *Adv. Mater.*, 2024, 2406608.

127 D. Verma, T.-C. Chen, B. Liu and C.-S. Lai, *Heliyon*, 2023, **9**, e22512.

128 Z. Dong, Q. Hua, J. Xi, Y. Shi, T. Huang, X. Dai, J. Niu, B. Wang, Z. L. Wang and W. Hu, *Nano Lett.*, 2023, **23**, 3842–3850.

129 D. Verma, B. Liu, T.-C. Chen, L.-J. Li and C.-S. Lai, *Nanoscale Adv.*, 2022, **4**, 3832–3844.

130 H. Xie, T. Yang, M. Xie, X. Liang, Z. Fang, Y. Ye, Y. Chen, Y. Wei, Z. Wang and H. Guan, *Laser Photonics Rev.*, 2024, **18**, 2301129.

131 J. Lee, S. Pak, Y.-W. Lee, Y. Cho, J. Hong, P. Giraud, H. S. Shin, S. M. Morris, J. I. Sohn and S. Cha, *Nat. Commun.*, 2017, **8**, 14734.

132 S. Lei, F. Wen, B. Li, Q. Wang, Y. Huang, Y. Gong, Y. He, P. Dong, J. Bellah and A. George, *Nano Lett.*, 2015, **15**, 259–265.

133 C. Fan, B. Dai, H. Liang, X. Xu, Z. Qi, H. Jiang, H. Duan and Q. Zhang, *Adv. Funct. Mater.*, 2021, **31**, 2010263.

134 Z. Chen, J. Huang, M. Yang, X. Liu, Z. Zheng, N. Huo, L. Han, D. Luo, J. Li and W. Gao, *ACS Appl. Mater. Interfaces*, 2023, **15**, 30504–30516.

135 J. Lai, H. Yang, K. Zhang, Y. Xiao, H. Zheng, Y. Zhong, J. Yu, Z. Chen and W. Zhu, *Opt. Commun.*, 2023, **537**, 129438.

136 M. Turunen, M. Brotons-Gisbert, Y. Dai, Y. Wang, E. Scerri, C. Bonato, K. D. Jöns, Z. Sun and B. D. Gerardot, *Nat. Rev. Phys.*, 2022, **4**, 219–236.

137 G. Konstantatos, M. Badioli, L. Gaudreau, J. Osmond, M. Bernechea, F. P. G. De Arquer, F. Gatti and F. H. Koppens, *Nat. Nanotechnol.*, 2012, **7**, 363–368.

138 C. Hu, D. Dong, X. Yang, K. Qiao, D. Yang, H. Deng, S. Yuan, J. Khan, Y. Lan and H. Song, *Adv. Funct. Mater.*, 2017, **27**, 1603605.

139 N. Huo, S. Gupta and G. Konstantatos, *Adv. Mater.*, 2017, **29**, 1606576.

140 J. Miao, W. Hu, N. Guo, Z. Lu, X. Liu, L. Liao, P. Chen, T. Jiang, S. Wu and J. C. Ho, *Small*, 2015, **11**, 936–942.

141 N. Li, Y. Wen, R. Cheng, L. Yin, F. Wang, J. Li, T. A. Shifa, L. Feng, Z. Wang and J. He, *Appl. Phys. Lett.*, 2019, **114**, 103501.

142 G. Sun, B. Li, J. Li, Z. Zhang, H. Ma, P. Chen, B. Zhao, R. Wu, W. Dang and X. Yang, *Nano Res.*, 2019, **12**, 1139–1145.

143 Y. Li, L. Huang, B. Li, X. Wang, Z. Zhou, J. Li and Z. Wei, *ACS Nano*, 2016, **10**, 8938–8946.

144 J. Song, L. Xu, J. Li, J. Xue, Y. Dong, X. Li and H. Zeng, *Adv. Mater.*, 2016, **28**, 4861–4869.

145 S. Lu, Y. Li and X. Zhao, *Phys. Chem. Chem. Phys.*, 2023, **25**, 19167–19174.

146 J. Li, X. Yang, Z. Zhang, W. Yang, X. Duan and X. Duan, *Nat. Mater.*, 2024, 1–13.

147 Y. Chen, C. Tan, Z. Wang, J. Miao, X. Ge, T. Zhao, K. Liao, H. Ge, Y. Wang and F. Wang, *Sci. Adv.*, 2022, **8**, eabq1781.

148 J. Lyu, S. Song and J. Gong, *ACS Appl. Electron. Mater.*, 2023, **5**, 4248–4253.

149 K. F. Mak, D. Xiao and J. Shan, *Nat. Photonics*, 2018, **12**, 451–460.

150 B. Chitara, E. Dimitrov, M. Liu, T. R. Seling, B. S. Kolli, D. Zhou, Z. Yu, A. K. Shringi, M. Terrones and F. Yan, *Small*, 2023, **19**, 2302289.

151 T. Li, T. Tu, Y. Sun, H. Fu, J. Yu, L. Xing, Z. Wang, H. Wang, R. Jia and J. Wu, *Nat. Electron.*, 2020, **3**, 473–478.

152 M. Yu, C. Tan, Y. Yin, J. Tang, X. Gao, H. Liu, F. Ding and H. Peng, *Nat. Commun.*, 2024, **15**, 3622.

153 Y. Gong, J. Lin, X. Wang, G. Shi, S. Lei, Z. Lin, X. Zou, G. Ye, R. Vajtai and B. I. Yakobson, *Nat. Mater.*, 2014, **13**, 1135–1142.

154 Y. Yoo, Z. P. Degregorio and J. E. Johns, *J. Am. Chem. Soc.*, 2015, **137**, 14281–14287.